UNIVERSITAT POLITÈCNICA DE VALÈNCIA

_ TELECOM ESCUELA TÉCNICA VLC SUPERIOR DE INGENIERÍA DE TELECOMUNICACIÓN

UNIVERSITAT POLITÈCNICA DE VALÈNCIA

School of Telecommunications Engineering

Electro-optical modulation based on transparent conducting oxides integrated in silicon photonics

End of Degree Project

Bachelor's Degree in Telecommunication Technologies and Services Engineering

AUTHOR: Salom Meló, Néstor

Tutor: Sanchis Kilders, Pablo

Experimental director: NAVARRO ARENAS, JUAN

ACADEMIC YEAR: 2022/2023

Resumen

La electrónica está alcanzando su límite en cuanto a velocidad y miniaturización se refiere. Como alternativa se proponen los circuitos fotónicos integrados (PICs). El objetivo de este trabajo fin de grado (TFG) es analizar y diseñar dispositivos de modulación electro-óptica basados en tecnología de óxidos transparentes conductores (TCOs) integrados en fotónica de silicio, concretamente centrándose en el uso de *indium tin oxide* (ITO). Este tipo de óxido semiconductor permite tunear la permitividad de forma que es posible trabajar en un régimen conocido como ENZ (*Epsilon-near-zero*), en cual la parte real de la permitividad es cercana a cero. De esta forma, las prestaciones de modulación pueden mejorarse de forma significativa en términos de eficiencia energética y velocidad de conmutación. Teniendo esto en cuenta, el dispositivo diseñado en este TFG consiste en un modulador híbrido de ITO/Si de amplitud y fase que funciona debido a las variación del índice complejo en una estructura capacitiva. Además se ha fabricado una muestra con ITO la cual se ha medido obteniendo unos resultados acorde con lo esperado según las simulaciones.

Resum

L'electrònica està arribant el seu límit quant a velocitat i miniaturització es refereix. Com a alternativa es proposen els circuits fotònics integrats (PICs). L'objectiu del treball fi de grau és analitzar i dissenyar dispositius de modulació electro-òptica basats en tecnologia d'òxids transparents conductors (TCOs) integrats en fotònica de silici, concretament centrant-se en l'ús del ITO. Aquest tipus d'òxids permet personalitzar la permitivitat de manera que és possible treballar en un règim conegut com ENZ (Epsilon-near-zero) en qual la part real de la permitivitat és propera a zero. D'aquesta manera, les prestacions de modulació poden millorar-se de manera significativa en termes d'eficiència energètica i velocitat de commutació. El dispositiu dissenyat consisteix en un modulador híbrid d'ITO/Si d'amplitud i fase el qual funciona gràcies a les variació de l'índex complex de l'estructura mitjançant l'aplicació d'un voltatge de polarització en una estructura capacitiva. A més s'ha fabricat una mostra amb ITO la qual s'ha mesurat obtenint uns resultats d'acord amb l'esperat segons les simulacions.

Abstract

Electronics is reaching its limits in terms of speed and miniaturization. As an alternative, photonic integrated circuits (PICs) are proposed. The aim of this thesis is to analyse and design electro-optical modulation devices based on transparent conducting oxides (TCOs) technology integrated in silicon photonics, specifically focusing on the use of ITO. This type of oxides allows tuning the permittivity so that it is possible to work in a regime known as ENZ (Epsilon-near-zero) in which the real part of the permittivity is close to zero. In this way, modulation performance can be significantly improved in terms of energy efficiency and switching speed. Thus, this TFG's designed device consists of a hybrid ITO/Si amplitude and phase modulator which works by varying the complex index of a capacitor-type structure through the application of a bias voltage. In addition, a sample has been fabricated with ITO which has been measured, obtaining results in accordance with the simulations.

Table of contents

Chapter 1. Introduction

1.1 Motivation

1.1.1 Silicon PICs and hybrid integration

In digital logic circuits, switching speed is a critical factor for proper performance, with today's applications requiring switching speeds of less than 100 ns (high switching speed) to meet the requirements of ultra-high density information processing and storage. Radio frequency (RF) bandwidth and power consumption, as far as traditional electronics are concerned, are limited by the RC product which is proportional to the scale of the gate capacitor in CMOS electronics. Efforts to try to improve the performance of these switching electronics during the past decades have focused on reducing the CMOS size, but recently there is a raising concern that component reduction is reaching its limit. Because of this, one of the most strongly technological alternatives is the integrated silicon photonics, which has the potential to be the basis for the next generation of ultrafast all-optical networks and photonic central processing units, a technology already under development that aims to improve the performance of the elements of silicon electronics [1].

Integrated photonics refers to the technology and field of study that focuses on the manipulation and control of light on a chip-scale or integrated circuit platform. It involves the integration of various optical components, such as waveguides, modulators, detectors, filters, and lasers, onto a single chip, a silicon substrate in the case of silicon-on-insulator (SOI) photonics. In integrated photonics, light is used to carry and process information, similar to how electrons are used in traditional electronics. The integration of multiple optical components onto a single chip allows for the creation of complex photonic devices that can perform various functions, such as optical communication, sensing, signal processing, and computing. These devices can offer advantages such as high-speed data transmission, low power consumption and immunity to electromagnetic interference [2].

But the main use and advantage of integrated photonics is the ability to work with a very wide bandwidth, thus allowing the transport of larger amounts of information at high light frequencies, of around 200 THz. Thus, transition from electronics to photonics will be able to ease the problems that arise in electronics when working with high transmission speeds (high energy dissipation). Indeed, this is mainly a physical problem; as the frequency of an electronic signal increases, the impedance of the conductor does it too, i.e., taking as a reference the classic coaxial cable, the attenuation of the cable is greater when working at higher frequency, limiting the use of electronics to close environments (tens of meters). On the other hand, photonics works with optical signals at wavelengths in which the materials are practically transparent (0.5 - 2 μm), thus greatly reducing propagation losses, allowing uses of even kilometres [2].

The use of silicon as a base material has been forged over the years. Silicon is an indirect bandgap semiconductor; it makes an ideal candidate to become the basis of most PICs, mainly due to its implementation as a wire (waveguide) since it has relatively weak non-linear effects [3] and the low propagation losses of silicon-based optical devices operating at the third window of communications [4]. In addition, silicon allows any type of planar PIC geometry to be realized in well-stablished silicon foundries and, thus, it is suitable for mass production.

However, silicon remains an all-passive semiconductor and in order to provide complex active functionalities to PICs (laser sources for example), other materials need to be integrated in the SOI platform. One of the first material families that were proposed to provide active effects to the SOI platform were the III-V (GaP, InP, GaAs [5]) compounds, which form direct-bandgap semiconductors. Today, a very large variety of efficient optical materials including functional oxides, Mott insulators, ferroelectrics, chalcogenides, polymers, carbon-based materials, nano and metamaterials, are considered in the framework of the SOI platform [6].

1.1.2 Benefits of transparent conductive oxides for silicon PICs

In the previous section the use of silicon in integrated photonics has been argued but its electro-optical effects are weak [7], being so its nonlinear effects also weak. Thus, in order to achieve PIC components with active behaviour, such as all-optical or electro-optical modulators, there is the need to integrate different elements with silicon, so that the resulting composition does possess them. In this research work we highlight the possibilities of transparent conducting oxides as ENZ materials. Recently it was shown as the possibility of obtaining very intense refractive index modulations in the hybrid SOI platform [8].

Indeed, ENZ materials have been established as novel path for integrated photonics and nanophotonic devices [9]. They are characterized by having a real permittivity which go through zero or being less than unity and close to zero in the case of NZI (near-zero index) materials. Thus, when the real permittivity is vanishing-small, the index change with power (n_2, non-linear index coefficient) varies considerably [10]. When this occurs, at the denominated ENZ point or ENZ condition, it takes place a large increase in the local electric field and the nonlinear effects may be greatly intensified [1].

In slot-like waveguide architectures, light tends to propagate tightly confined through the lower effective index areas. Similarly, in hybrid SOI structures loaded with ENZ materials, the light propagation occurs in special modes that provide very strong modal confinement to the light. Such modes are called ENZ modes and their main characteristic is that a large fraction of light is confined in the zero-permittivity region [11]. This allows the effective index of the hybrid waveguide to be greatly perturbed by changing the index of the ENZ material around its ENZ point, thus enabling strong optical modulation.

There are several materials with the possibility of achieving zero real permittivity and, therefore, considered as ENZ materials, some of them being natural while others are artificial. As for the artificial ones, they are called metamaterials, which obtain the ENZ effect thanks to the combination of their material and structural properties [12], because they are composed of elements with sub-wavelength scales (dimensions smaller than the wavelength of the light used) in one or more dimensions [13]. Within natural materials, one group that stands out are the transparent conductive oxides (TCOs). Such materials can be CMOS-compatible, and its ENZ can be tuned in the near-infrared (NIR) window with low losses [8].

TCOs are a set of materials among which indium tin oxide (ITO), doped cadmium oxides (CdO), aluminium-doped zinc oxides (AZO) and indium oxide (In_2O_3), and others, stand out [8][14]. As mentioned above, TCOs are the most widely used materials to achieve the ENZ effect in integrated photonics. This is due to their electron concentration, which is large enough to tune the ENZ at 1550nm (C-band, normally used in integrated silicon photonics) but small enough not to have many losses like traditional noble metal plasmonics [15]. Thus, TCOs are considered low-loss materials due to their carrier concentration. In addition, they have other interesting possibilities such as the ability to continuously tune of the material's optical constants through the adjustment their carrier concentration through all-optical or electro-optical mechanisms that can be built in the PICs [1].

1.1.3 TCO-based electro optic modulators

Optical fiber communication and silicon-based microelectronics are the basis of the current information technology revolution. However, in the high-speed information age, computing is nowadays facing bottlenecks of speed. Thus, silicon-based optoelectronics has emerged as the pivotal technology to overcome these challenges due to the possibility of integrating complete optical circuits and electronic control logic on a single chip, with the advantages of electronics and optics, thus potentially reducing the speed and energy consumption of the device, a priority objective in almost all research fields. Indeed, electro-optic devices typically offer high bandwidth and high speed [16].

A key component in the development of silicon optoelectronics is the electro-optic modulator. Classical silicon-based electro-optic modulators need very long devices (in the order of hundreds of micrometres) to achieve the required performance [17]. For example, the most straightforward technology is based on microheaters, a miniaturized heating system that generates heat through Joule heating, that can be implemented with silicon-only waveguides. The problem with these relatively simple silicon modulators is that, since they speed is usually very slow in the order of microseconds[18].

This is where the TCO-based electro-optic modulators come in, which have emerged as an interesting new research path to achieve high-speed information technology requirements in an ultra-compact device architecture [19]. This can be achieved thanks to the unique characteristics of TCOs, due to the ENZ-tuning of their optical properties commented above [20], as well as its potential low losses [21]. In addition, TCO-based electro optic modulators can allow amplitude modulation, phase modulation or both at the same time [22]. Following this trend, the modulator presented in this work allows amplitude and phase modulation.

Such device operates with a metal-oxide-semiconductor (MOS) capacitive structure. The inner working of such a device can be understood with the Drude model (which will be discussed later); since the real and imaginary part of the permittivity of ITO vary as a function of the material's electron concentration, the ENZ operation can be modulated by tunning the accumulating charges by biasing the capacitor (see Fig. 1.1 for an schematic explanation). This gives the material radically different optical behaviours, allowing it to act as a dielectric or as a metal. Such rich behaviour is important to achieve phase-amplitude modulation in a single device.

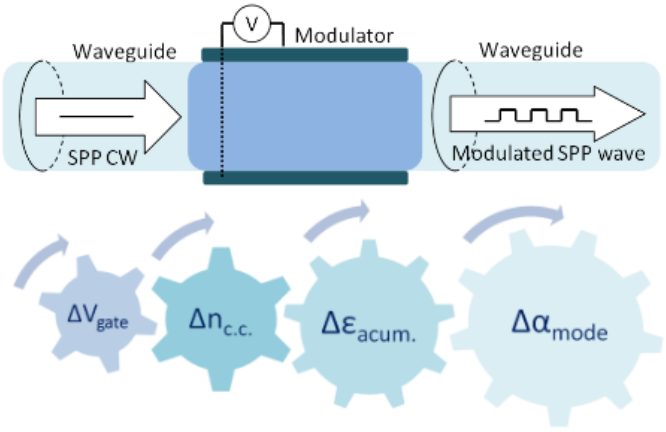

Figure 1.1. General concept of a TCO modulator for hybrid photonic/electronic circuits [23]

ITO (like the other TCOs) can be used to constitute a MOS-like capacitor, operating as the semiconductor. There are many configurations possible that can be found in literature, i.e., the ITO layer and the oxide layer can be sandwiched between two silicon (Si) layers, resulting in a device similar to a slot waveguide [24]. The second structure consists of two metal layers between which both the ITO and the oxide are sandwiched, thus forming a metal-dielectric-metal and so a field-effect modulator [25] [26]. The last structure is based on a Si guide on which the ITO, the oxide is deposited, and the metal layer are then placed on top. The bias voltage is applied between the ITO and the metal [27]. In terms of the advantages and disadvantages of each, the first and third structures integrate perfectly with conventional Si waveguides, thus offering high coupling efficiency (low coupling losses). The second configuration, in addition to the classic waveguides, integrates easily with any type of waveguide. The negative point of this structure is that it has very high insertion and coupling losses, thus ruling out this option when it involves a standard Si waveguide. This type of modulator, regardless of the configuration, works only for TM

polarisation. Of the three options, the structure to be developed in this work will be the third one in which HfO_2 will be used as the oxide and gold (Au) as the metal. This will be discussed further in chapter 2. A summary of the possible configurations can be found in Fig. 1.2.

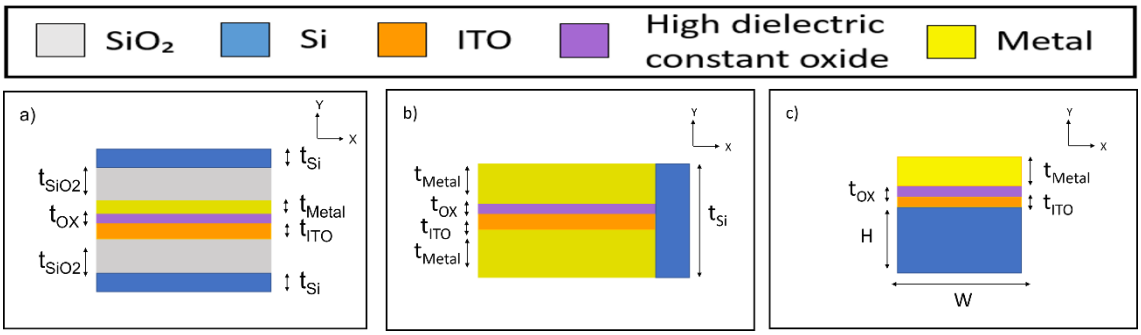

Figure 1.2. Waveguide configurations for enabling TCO modulators. a) Shows the first configuration (SiO_2/ITO/Oxide/SiO_2). b) Shows the second configuration (Metal/ITO/Oxide/Metal). c) Shows the third configuration (Si/ITO/Oxide/Metal)

1.1.4 Optical modulation role in photonic neural networks

Photonics, thanks to its unique properties and benefits, has been used in a wide range of applications. Research focused on new materials (such as the aforementioned TCOs) has opened the door to further application fields such as quantum, and photonic neural networks.

In this context, a neural network is a computational model inspired by the workings principles of the human brain. Also known as artificial neural networks, they are information processing systems consisting of an interconnected units called "neurons" or "nodes" that work together to solve problems or perform specific tasks. Each neuron in an artificial neural network receives inputs from other neurons through weighted connections. These connections represent the strength or importance of the signal that one neuron transmits to another. Each neuron applies an activation function to the inputs received and produces an output that is sent to other neurons.

The structure of a neural network can vary in complexity and design but is generally divided into layers. The input layer receives the input data, the output layer produces the final results, and intermediate layers, known as hidden layers, process and transform the information as it propagates through the network. The main features are massive parallelism, learning capability, distributed representation and computation, adaptability, information processing, fault tolerance and low energy consumption. [28].

Traditionally, neural networks have been implemented using electronic-based processors, but a bottleneck has been reached. This bottleneck is caused by unsustainable performance growth. The demand for high-performance computing has increased considerably in recent years, mainly due to the increasing development of artificial intelligence and its tools. This increase in demand has resulted in an increase in energy consumption, which has become the main constraint for the practical implementation of neural network electronics. The explanation for this comes when the inner workings of a neural network are understood. In it, computations are usually treated as matrix multiplications and the speed and energy efficiency of electronic technology is limiting. In addition, other limiting aspects for this technology is the bandwidth; the interference of electronic signals with each other and limits maximum number of interconnected cores [29], which in the end severely limits the parallelisation of the processes [30].

The use of photonics has been proposed as another approach for implementing neural networks. The change from using electronic to photonic processors, photons instead of electrons, brings the unique characteristics of photonic technology such as ultra-wide bandwidth, ultra-fast processing frequency and ultra-low power consumption [30]. It also has the possibility to work with a higher

number of cores compared to electronic technology, which allows parallelisation of computing processes and thus reduces processing time. In addition, photonics allows a high level of parallelism over the same physical channel and therefore a higher transmission speed, as several wavelengths can travel through the same core thanks to wavelength division multiplexing (WDM) [31]. Such ultra-fast information processing opens the door to improvements in fields such as scientific computing [32]. They also provide an effective way to support large-scale integration for on-chip all-optical computing chips [30].

Photonic devices can be used to neural networks in the two key processes: the activation function and the weighting of the information carried by each neuron [32]. Both processes have been mentioned earlier in this section when briefly describing the functioning of a neural network. Among the photonic technologies, the one that stands out for its practical implementation in this context is the one of silicon optoelectronic modulators. Indeed, silicon-based optical modulators, such as the one proposed in this project, can be used to design activation function for photonic neural network [31].

This demonstrates the present and future importance of the technology of optoelectronic modulators, and photonic technology in general, for neural networks, and constitutes one of the most attractive research fields to apply directly the results of this work.

1.2 Objectives

The main objective of this work is to design an electro-optical amplitude and phase modulator using a hybrid TCO/Si device. The device acts as modulator by varying the accumulated charge in a MOS-like capacitor structure that incorporates the TCO.

As for the specific objectives:

- Design an efficient hybrid electro-optic modulator at the C-band of telecommunications using ITO.
- Design of an arrayed multilength modulator from the implementation of various hybrid base ITO/Si modulators to increase the expressivity.
- Propose an improvement of the base modulator by replacing ITO with high-mobility TCOs such as CdO.
- Fabricate of a test device at the NTC (Nanophotonics Technology Center) in the context of an on-going international collaboration and testing and measurement of the device.

1.3 Methodology

In order to achieve the objectives presented above, the steps presented in this section will be followed:

1. First, the ITO will be modelled as a function of the bias voltage using the Drude model. For this purpose, the Matlab code that simulates the Drude equations and the biasing of the MOS-like capacitor structure will be used.
2. Afterwards, the complete modulator structure will be designed and simulated in FEMSIM, a tool contained in the RSoft's CAD photonic simulation environment. In this way, the optical behaviour of the overall structure can be explored and optimized.
3. By exporting the FEMSIM data (effective index of the modes) back to Matlab, the losses and phase shift of the device can be processed and obtained. In this way, and through the use of two figures of merit (FOMs) defined for this work, the thickness of the oxide and other design parameters that make up the structure can be optimised so that the best possible performance can be extracted.
4. Subsequently, a design of an arrayed multilength ITO/Si modulator, a series of modulators are concatenated and perform independently with their own biasing voltage,

is carried out. FEMSIM is used to obtain the effective indices of the device and Matlab is used to process the data and obtain the of the devices performance (losses, phase shift, etc.). Such arrayed modulator structure greatly increases the modulation expressivity when compared with a single modulator.

5. Next, all the initial process described above was carried out, but replacing the ITO layer with CdO, another TCO with greater mobility (and therefore better performance).
6. Finally, a hybrid waveguide loaded with ITO was fabricated to obtain preliminary results for the final design.

1.4 Contribution to SDG

To conclude Chapter 1, it only remains to comment on what SDGs the work that has been developed contributes to. The design of the modulator is strongly linked to Goal 9: industry, innovation and infrastructure. This is due to the fact that the development and research that has been carried out has as its final objective the possible practical implementation in the professional field and therefore in industry. The aim of this study is to develop a new technology and to promote its possible use.

Chapter 2. Design of the ITO/Si modulator

2.1 Principle of operation of the proposed modulator

The device to be developed is an ITO/Si hybrid phase-amplitude modulator whose schematic structure, both in 3D and 2D, can be seen in Fig. 2.1. The device has a Si guide of standard size (500 nm wide and 220 nm high) on which are deposited, in that order, an ITO layer (10 nm thick); an oxide layer, in this work the one chosen for its properties is HfO_2 (initially 10 nm thick, although the optimum thickness will be determined later); and finally a gold (Au) layer with a thickness of 100 nm. This entire structure is mounted on a SiO_2 base. The choice of HfO_2 as an insulator is due to its high permittivity, which allows the device properties to be tuned by voltage without reaching the oxide's breakdown potential, which in this case is around 10V [33].

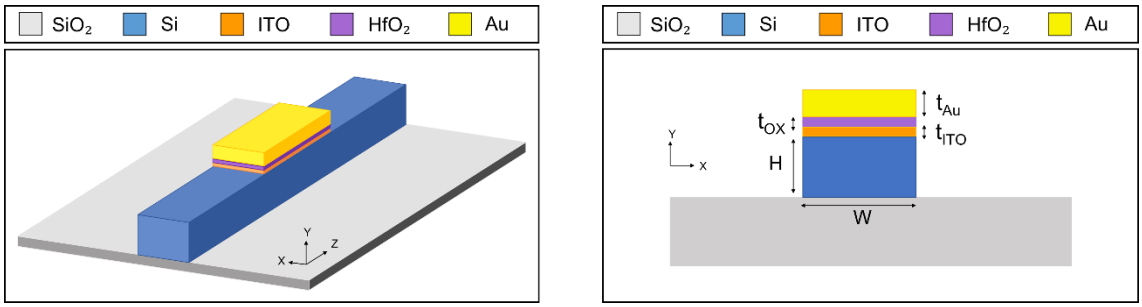

Figure 2.1. Structure of the ITO/Si hybrid phase-amplitude modulator

As for the principle of operation, such device exploits at the same time two unique features of the modulator, the plasma dispersion effect, and the enhancement of the absorption effect of the ENZ, achieving phase and amplitude modulation. The plasma dispersion effect contributes in changing the refractive index and resonance wavelength of the hybrid Si waveguide by manipulating the carrier concentration in the device. In this case, this would be done by varying the carrier concentration of the ITO (N_{ITO}). In the designed structure only the fundamental mode TM will be considered because the main field component is in the y-direction (E_Y). The enhancement of the absorption is achieved when the ITO's real permittivity is tunned near the ENZ resonance and the light is tightly confined inside the lossy ITO film.

The device is biased with a direct voltage causing the creation of a new region inside the ITO with a surplus of electrical charges called the accumulation layer. This is formed by the free carriers of the ITO that accumulate near the interface with the oxide when the voltage is applied. Thus, since the carrier density is directly related to the complex permittivity, the effective rate of the modulator can be changed by an external bias voltage.

By varying the voltage applied to the structure, three operating points can be found as a function of the indices as shown in Fig. 2.2. When no voltage is applied, it is in a steady state and the phase contrast, and the propagation losses are low (low effective κ). Thus, the transmission is maximal. The second state is amplitude modulation, the device is operated in around the centre of the ENZ resonance (approximately between 2.5 V and 4.5 V in Fig. 2.2), a state in which the losses are maximal. At the centre of the ENZ resonance the phase difference is zero and, thus, pure amplitude modulation can be achieved. The last state is phase modulation, which is tuned with voltages that configure the device off the ENZ zone (approximately between 2.5 V and 2 V and between 4.5 V and 5 V in Fig. 2.2). This allows a phase difference to be obtained with minimum losses [34]. In this way, the various states can be tuned depending on the voltage with which it is polarised. Mixed states enable continuous variable phase-amplitude modulation. In the next section, the behaviour of the ITO near the ENZ will be discussed in more detail.

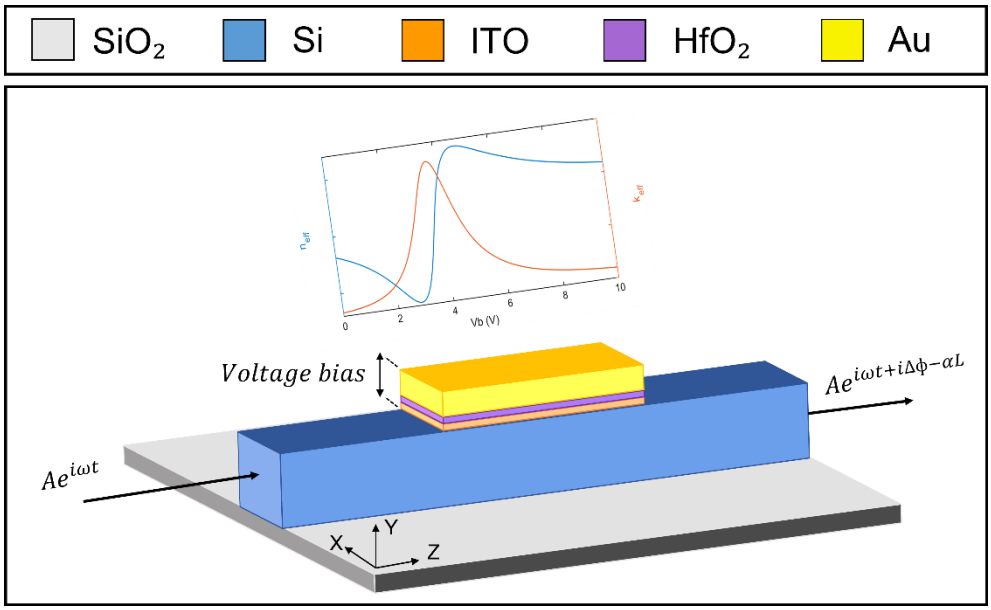

Figure 2.2. Structure of the ITO/Si hybrid phase-amplitude modulator with the effective index variation

2.2 Modelling of the ITO permittivity near the ENZ

In this section we intend to model the permittivity of the ITO near the ENZ zone. For this purpose, the structure presented in the previous section (Fig. 2.1) will be considered. For this work the ITO has been modelled using the Drude model [35]:

$$\varepsilon = \varepsilon_\infty - \frac{N_{ITO} e^2}{\varepsilon_0 m_0} \cdot \frac{1}{\omega^2 + i\omega\Gamma} \tag{2.1}$$

where ε_∞ is the high-frequency permittivity, N_{ITO} is the electron concentration in the ITO, ε_0 is the vacuum permittivity, m_0 is the effective mass (rest electron effective mass times electron mass), ω is the angular frequency and Γ is the electron damping factor.

For the implementation of the model the Matlab tool has been used, in which the following parameters have been set: $\varepsilon_\infty = 3.66$ [36]; $m_0 = 0.49 \cdot m_e$ [36] where m_e is the electron mass; ω adapted to work at 1.550 nm wavelength; and the damping factor Γ which can be defined as:

$$\Gamma = \frac{e}{\mu \cdot m_e} \tag{2.2}$$

It depends on the mobility (μ) which is set to $20 \cdot 10^{-4}\ m^2 \cdot V^{-1} \cdot s^{-1}$ [36]. In this way the complex permittivity and complex refractive index of the material is obtained in Matlab as a function of the ITO electron concentration (N_{ITO}), which is explored between $0.5 \cdot 10^{21}$ and $1.5 \cdot 10^{21}\ cm^{-3}$, typical values for N_{ITO}. In this way, the optical behaviour of the ITO as a function of carrier concentration is obtained. Fig. 2.3 shows the three behaviours experienced by the material, behaving as a dielectric for N_{ITO} lower than $0.85 \cdot 10^{21}\ cm^{-3}$ (real part higher than the imaginary part of the complex index), as a metal for higher concentrations (real part lower than the imaginary

part of the complex index) and as an ENZ element at a N_{ITO} at about $0.85 \cdot 10^{21}\ cm^{-3}$ (crossover between real and imaginary part, same value at 1.550 nm wavelength).

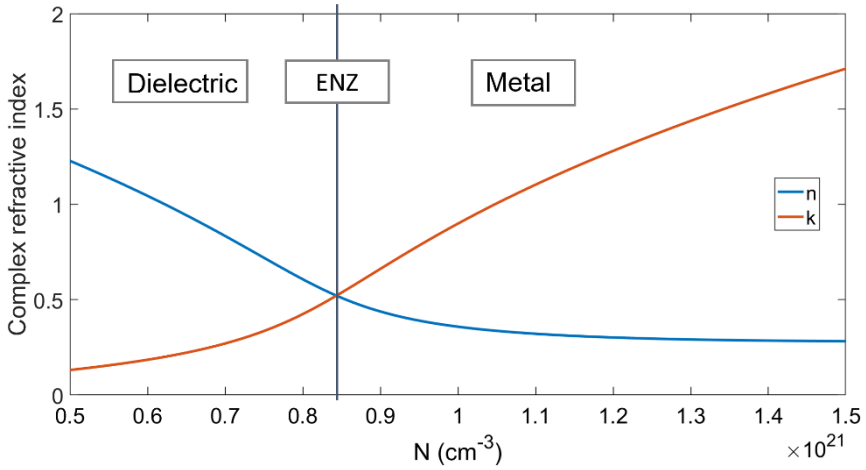

Figure 2.3. Complex index vs carrier concentration for ITO.

This point ($N_{ITO} \simeq 0.85 \cdot 10^{21}\ cm^{-3}$) coincides with the point where the real part of the complex permittivity crosses through zero (Fig. 2.4), demonstrating the ENZ criteria.

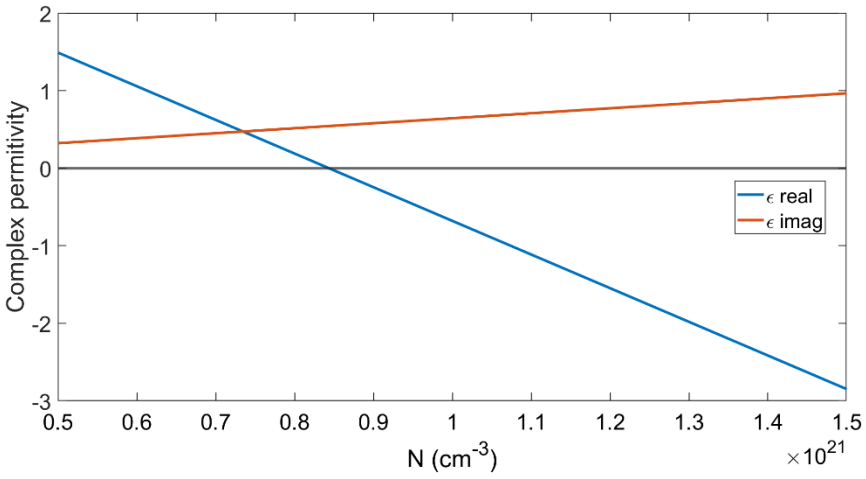

Figure 2.4. Complex permittivity vs carrier concentration for ITO.

Since the objective is to obtain the variation of the ITO complex index by voltage, a capacitor model relating the voltage to the ITO carrier concentration needs to be introduced. The model used in this work is the plane parallel capacitor equation [35] with HfO_2 as capacitor's oxide film.

$$N_{AcL} = N_0 + \Delta N \tag{2.3}$$

$$\Delta N = \frac{\varepsilon_0 \cdot \varepsilon_{HfO2}}{e \cdot t_{HfO2} \cdot t_{AcL}} (V - V_{FB}) \tag{2.4}$$

Thus, a new layer is considered, called the accumulation layer, which is actually part of the ITO layer but, when subjected to voltage, its optical constants can be modified. In this way, the carrier concentration is subjected to voltage-dependent changes. Thus, a new layer (AcL) will have the base carrier concentration (N_0) altered by a specific accumulation of charges that are given by the capacitor configuration (ΔN). This specific accumulation can be seen in equation 2.4 where: ε_{HfO2} is the permittivity of HfO_2; t_{HfO2} is the thickness of the HfO_2 layer; t_{AcL} is the thickness of the accumulation layer; and $(V - V_{FB})$, also named as V_b, is the voltage applied to the capacitor.

The 2D structure of the capacitor can be seen in Fig. 2.5.

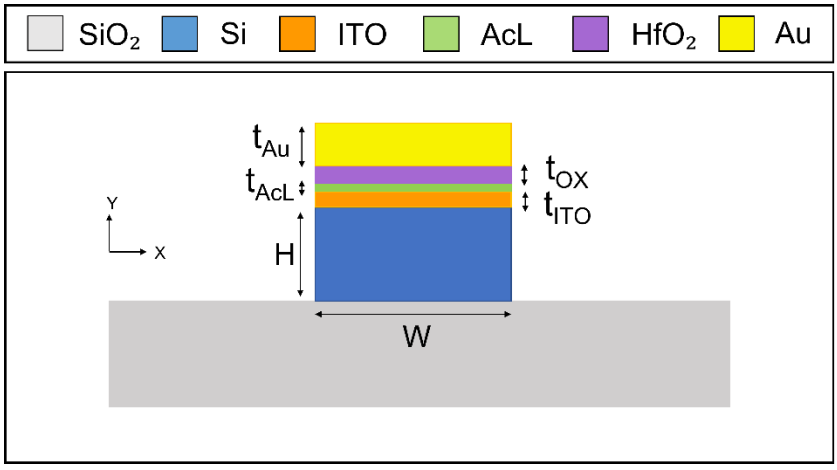

Figure 2.5. Structure of the hybrid Si/ITO capacitor with the accumulation layer.

As for the implementation of the model in Matlab, the initial design has been considered where $N_0 = 3.5 \cdot 10^{26}\ m^3$ [35], $t_{HfO2} = 10\ nm$ [14], $\varepsilon_{HfO2} = 25$ [35], $t_{AcL} = 1\ nm$ [14] (leaving the base ITO thickness at 9 nm). Leaving V_b as a variable between 0 and 10 V, the plot gives Fig. 2.6, where it can be seen that the ENZ working point happens at approximately 3.5 V for the specified capacitor. These curves of the real and imaginary part of the index of the ITO will be exported from Matlab to be imported into the RSoft program. In RSoft's FEMSIM tool, the effective index of the complete device and the modes propagating along the guide will be obtained. This will be discussed in the next section.

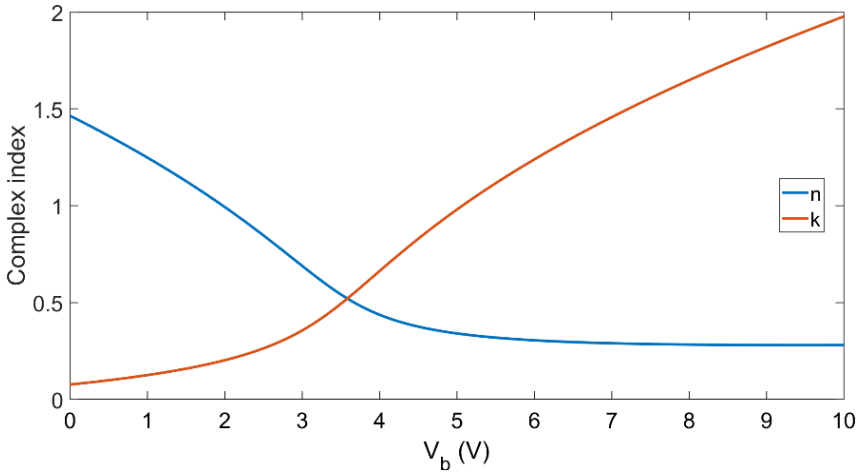

Figure 2.6. Complex index vs bias voltage (V_b).

2.3 Performance analysis of the device

2.3.1 Estimation of the complex effective index

In this subsection, the complex effective index of the modulator will be obtained. This is essential to continue with the study of the device. For this purpose, as mentioned in the previous section, RSoft will be used. RSoft is a software for the design and simulation of photonic elements and devices. There are several tools within this software, but to obtain the effective indices of the device, only one tool called FEMSIM will be used. FEMSIM is a generalized mode solver based on the Finite Element Method. The main function of FEMSIM is to obtain the effective indices and modes of a structure, so it will also be of use later in the analysis of modal field distribution.

Two main steps have been necessary for the simulation of the structure. The first of these steps was to input of the device's geometry in the CAD environment. In this way, Fig. 2.5 above was reproduced in RSoft. The next step was to export the data concerning to the complex index of the ITO and its variation with voltage to FEMSIM. For this purpose, these data were exported from Matlab to a plain text file and imported into the simulation software with the appropriate variables.

This way the simulation would be almost ready to be launched. In order to obtain greater precision in the study without investing an excessively long time in the simulation, a non-uniform mesh was applied to the geometry. Each segment (areas with different refractive index) of the total geometry is divided into smaller sections (like a mesh or net) and simulated. The higher the simulation accuracy, the more sections the background has to be divided into, which increases the simulation time exponentially. As the critical area of the study is where the ITO accumulation layer and neighbouring areas are located, the simulation needs much more precision inside such areas while other regions contribute less to the simulation. The result of this configuration with uniform meshing can be seen in Fig. 2.7. As can be seen, the mesh is much denser in the desired accumulation area.

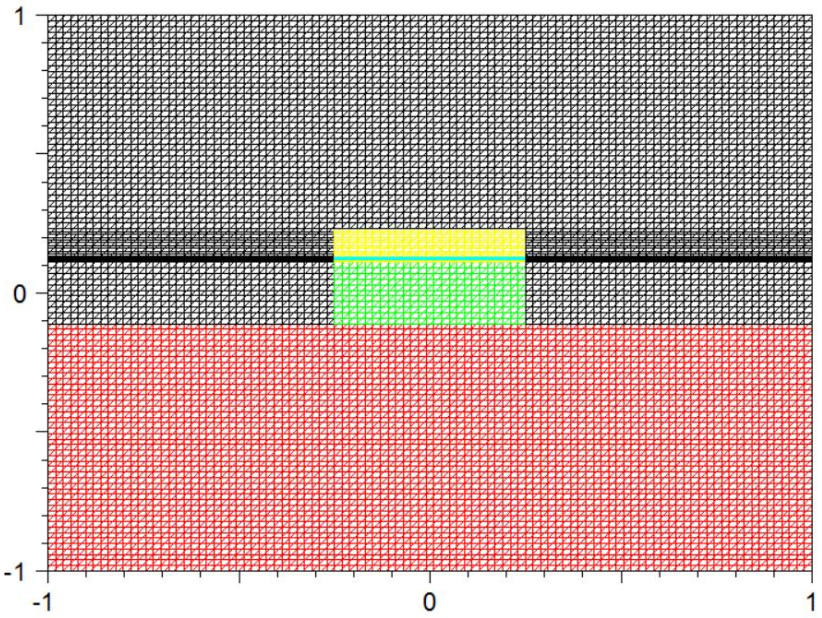

Figure 2.7. Non-uniform meshing used in the RSoft simulation

The simulation is then ready to be launched. From it, the complex effective indexes are obtained as a function of the voltage applied to the structure. After importing this data into Matlab, Fig. 2.8 clearly shows a typical sigmoidal-like real resonance and bell-like imaginary resonance. Following on from the conclusions drawn in section 2.2, for the ITO to behave like an ENZ

material, the applied gate voltage must be around 3.5 V. At this voltage, the structure would be found to be in the same condition as the ENZ material. At this voltage, the structure would also be working in the ENZ region, due to the fact that the imaginary part of the complex index (κ_{eff}, associated with the losses) is maximum. At this voltage the structure would have very high losses and light passing through the structure (light is confined in the ITO layer) will be attenuated. At this point the structure has a complex effective index of 2.647 + 0.183 j. In addition, the real part also has two peaks, in this case a maximum and a minimum. This representation of the complex effective index allows easy intuition of the amplitude and phase modulation of the device.

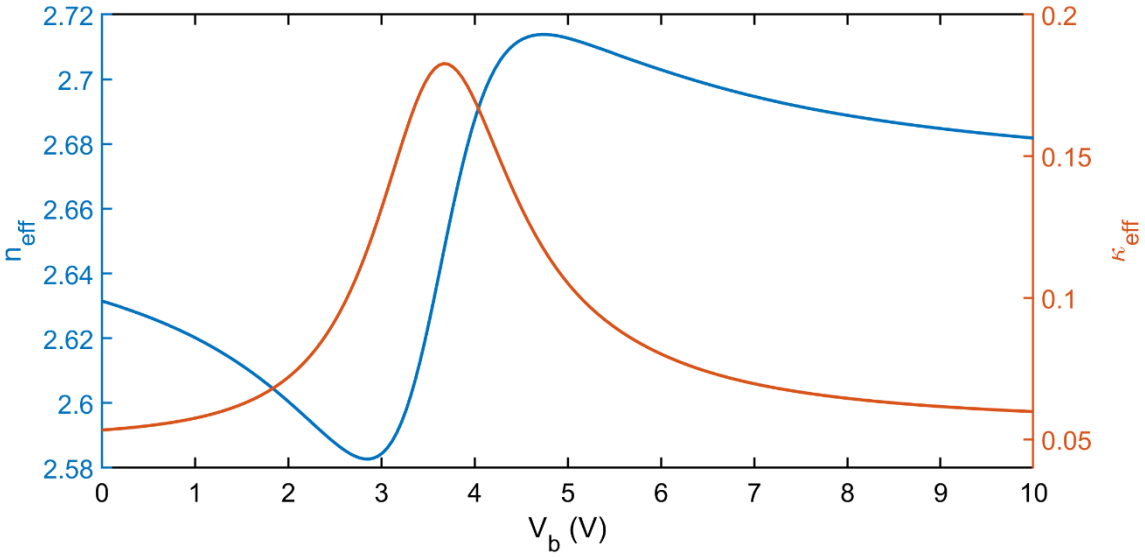

Figure 2.8. Evolution of the complex effective index of the structure versus voltage

This same procedure will be repeated later to obtain the optimum oxide thickness, because in this subsection we have worked with the oxide thickness initially set (10 nm).

With this, the operation of the device has been modelled. Based on the information obtained, a more exhaustive analysis of the operation of the modulator will be carried out in the following subsections.

2.3.2 Definition of Figure of Merits (FOMs)

In this subsection, the aim is to analyse the response and performance of the device based on a metric called Figure of Merit (FOM). The FOM is a quantitative value which is used to compare the performance of different structures in order to know which one is better. It is usually defined in such a way that the FOM is maximised when the device performs best. The FOM does not have a fixed general formula for all cases, but a particular formula is determined for each study.

In this work, two different FOMs will be defined considering two key variables: phase shift and losses. In this way, two different criteria will be used to analyse the behaviour of the device and therefore optimise it. The first of the formulas to be used is the FOM referring to the phase difference:

$$FOM^{\Delta\phi} = \frac{\Delta\phi}{\alpha} \tag{2.5}$$

where α is the propagation loss and Δϕ is the device phase shift per unit length whose equation is the following:

$$\Delta\phi = \frac{2\pi\left(n_{eff}(V) - n_{eff_0}\right)}{\lambda} \tag{2.6}$$

In this way, the behaviour can be analysed as a function of the voltage applied to the device, since, in addition to the phase shift, the propagation losses (α) also vary as a function of V_b. Similarly, the FOM applied to the losses is shown:

$$FOM^{\kappa} = \frac{ER}{\alpha_0} \tag{2.7}$$

This FOM, like the phase shift, also depends on the bias voltage, in this case due to the definition of ER, which is the difference between the propagation loss for each V_b and the loss when no voltage is applied (α_0). Having defined the two FOMS that will be used in this work, the next subsection will address the optimization of the device structure by reaching a compromise between the two FOMs.

2.3.3 Optimize FOMs with the oxide thickness

As mentioned, the two FOMs defined in the previous subsection will be used to determine the optimal device structure, specifically to obtain the oxide thickness (in this design it is HfO_2) that allows obtaining a maximum value of the FOMs with the lowest possible bias voltage. V_b is a critical element because a low voltage is essential for low power consumption and to avoid damage to the device. To proceed with the optimisation, the HfO_2 thickness has been modified between 5 nm and 25 nm in 5 nm intervals, and the FOMs have been obtained for each of these thicknesses. To do this, the analysis of subsection 2.3.1 was repeated in FEMSIM, setting the thickness at the values to be studied and obtaining the effective complex index for each possible modulator structure. Once these complex effective indices have been obtained, they have been exported to Matlab where the calculation of the different FOMs has been done.

The first analysis will be the one concerning the $FOM^{\Delta\phi}$ whose curves can be seen in Fig. 2.9 below. It can be seen that the maximum of the FOM seems to be independent of the oxide thickness, since all the curves have a similar peak value. However, there are other parameters that are dependent on the oxide thickness. As the oxide thickness increases, both the voltage at which the maximum point is achieved and the voltage range that can be applied to achieve the best response from the device, increase. In other words, the thicker the oxide, the flatter the response curve at the maximum point, but the more V_b required to reach the maximum point. In order to analyse the results, it is convenient to take into account that if the applied voltage is too high, the oxide's breakdown voltage can be reached [33], which would cause the device to break. In other words, a low voltage is of interest, as a lower voltage also means lower energy consumption.

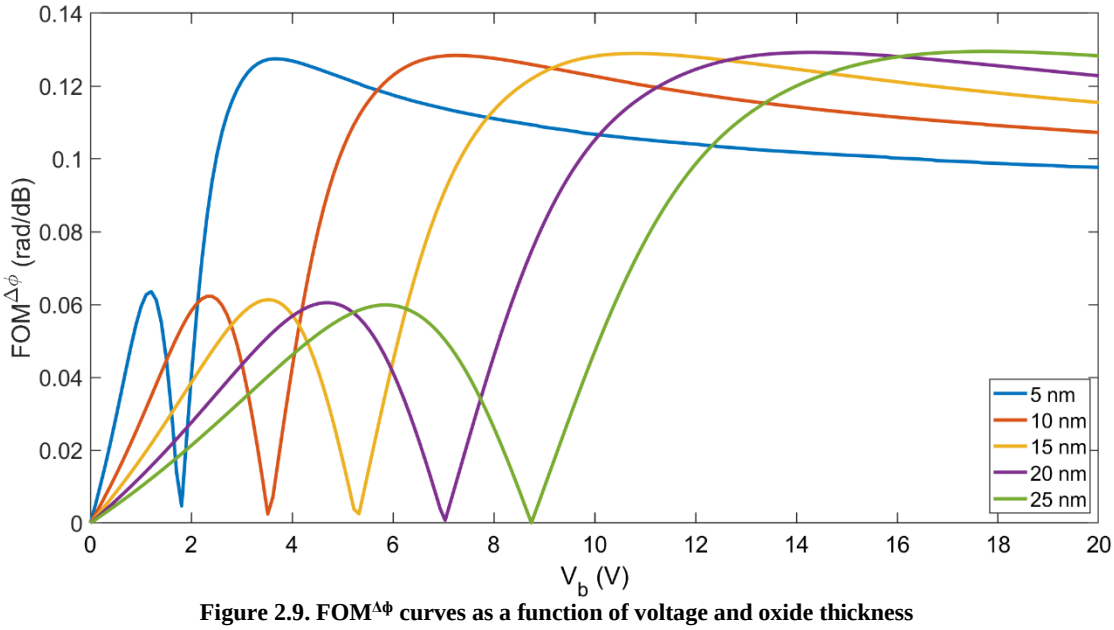

Figure 2.9. FOM$^{\Delta\phi}$ curves as a function of voltage and oxide thickness

We now proceed to study the FOM$^{\kappa}$. To do this, the same procedure has been followed as in the previous one, obtaining Fig. 2.10. From it we can obtain similar conclusions to the previous ones. In this case, the peak value of the FOM is not constant but the variation with thickness is minimal, being slightly higher for lower thicknesses. As with the FOM$^{\Delta\phi}$, as the thickness increases, the response becomes flatter and requires higher voltage.

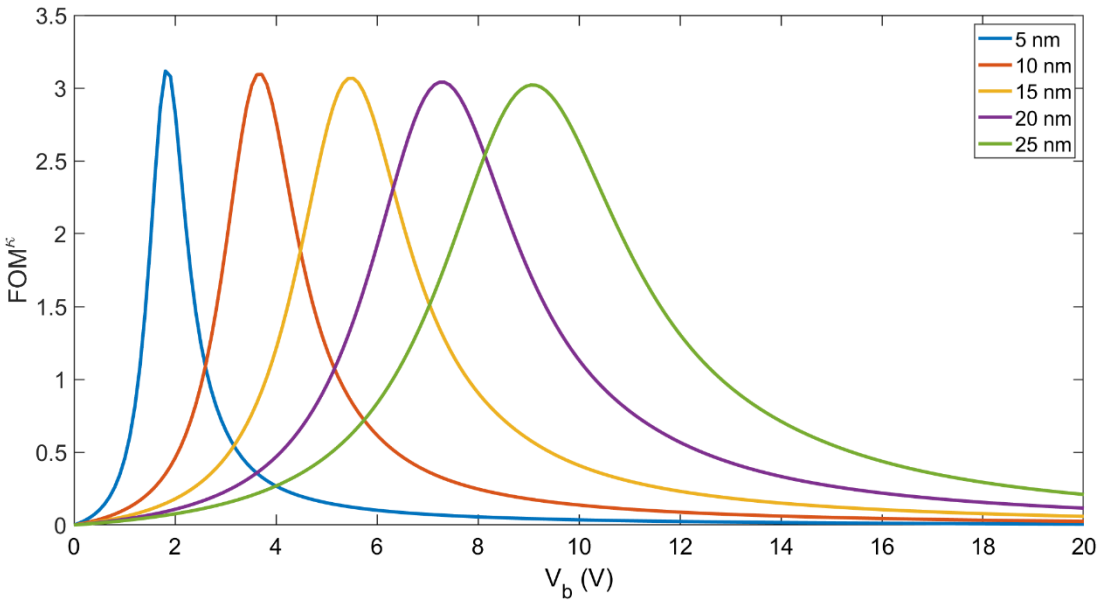

Figure 2.10. FOM$^{\kappa}$ curves as a function of voltage and oxide thickness

The two criteria will now be brought together. Due to the fact that all the thicknesses have identical peak values in the two FOMs, the applied voltage and the flatness of the response have to be considered. A narrower FOM response forces the system to be more accurate in biasing the device by voltage. As for the applied voltage, it is important to keep it as low as possible. This would make the device more attractive for possible further real implementations. Despite this and

considering the repercussions that an incorrect voltage would have on the performance, it has been decided to take 10 nm as the optimum and definitive thickness, since, although the V_b required is greater, a wider range of operation in the optimum zone is guaranteed. In this way, the voltage applied has a safety margin to guarantee correct operation. Furthermore, by considering not the smallest possible thickness but a slightly thicker one, it is an easier design to fabricate (e.g., avoiding electrical pinholes and other fabrication potential issues of thin film technology). Therefore, we can consider 10 nm as a compromise between energy efficiency, performance and manufacturability.

This determines the optimum thickness of the insulator layer of the device. Further analysis of the operating voltages and power consumption for this design will be covered in the following subsection.

2.3.4 Optimal operation voltages and energy consumption

In the previous subsection, the thickness of the insulator was set at 10 nm, so this subsection aims to analyse the operation of the device with this structure. Specifically, the aim is to determine the necessary voltage and power consumption at the optimal operating points, taking the $FOM^{\Delta\phi}$ and FOM^{κ} as a reference. The necessary voltage does not require any extra calculation with respect to the previous section, but the energy consumption does. To obtain the power consumption considering that the device behaves as a switch, the following equation is used [35]:

$$E_s = \frac{1}{2} C (V_1^2 - V_0^2) \tag{2.8}$$

where $V_1^2 - V_0^2$, is the switching state and C is the capacitance of the structure. For the study, the modulator is considered to switch between an initial state where the applied voltage is 0 V and the desired state where ΔV will only be affected by V_1. To determine the energy consumed by the switching between two states other than the resting state (V_0 = 0 V), it would only be necessary to subtract the energy consumption at each of the points. In order to obtain the C of the system, the following equation is applied [35]:

$$C = A \cdot \frac{\varepsilon_0 \cdot \varepsilon_{HfO2}}{t_{HfO2}} \tag{2.9}$$

where A is the area of the structure (500 nm x 1 µm), ε_{HfO2} is the permittivity of HfO_2 (ε_{HfO2} = 25) and t_{HfO2} is the thickness of the HfO_2 layer (t_{HfO2} = 10 nm). A graphical visualisation of these results can be seen in Fig. 2.11.

Analysing the peak values of both FOMs, it is concluded that to obtain an optimal operation in terms of losses, it is necessary to inject 3.7 V to the device, which would cause an energy consumption of approximately 75 fJ. On the other hand, to work at the point of maximum phase shift, it is necessary to bias the device with 7 V, obtaining an energy consumption of 270 fJ. All these data, as already explained, are based on an initial switching state with an applied voltage of 0 V. These energy consumption values are reasonable to studies of similar structures [35] [37] [19].

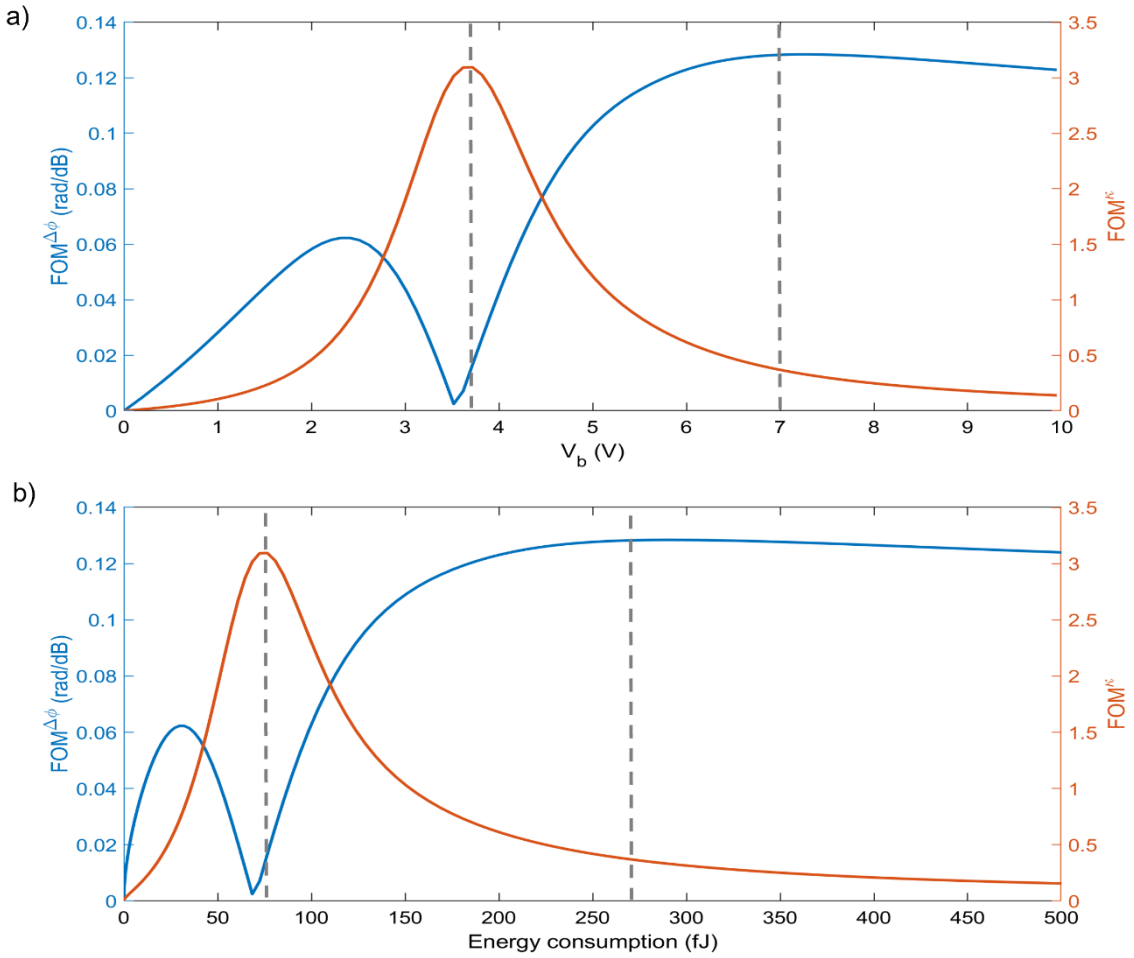

Figure 2.11. Plot of the two FOMs defined as a function of bias voltage (a) and energy consumption (b)

2.3.5 Estimation of the modulation speed

In this subsection, the aim is to estimate the modulation speed of the capacitor. This speed can be defined as the bandwidth or frequency at which the hybrid modulator works. To obtain it, the following capacitor equation [38] will be used:

$$f = \frac{1}{2\pi RC} \tag{2.10}$$

where R is the resistance of the device and C is the capacitance of the structure obtained in the previous subsection. As can be seen in equation 2.10, the working frequency of the device depends only on the RC product. This product is inversely related to the frequency, i.e., as the RC product increases, the frequency decreases and vice versa.

As for the resistance used, it has been considered around 700 Ω as it is the one applied in a structure similar to the one designed in this work [39]. This gives a frequency close to 20 GHz. This result is also consistent with other works reported in the literature [35].

2.3.6 Analysis of modal field distribution

In this subsection, the modal field distribution of the structure will be analysed as a function of the applied bias voltage. Specifically, the structure will be analysed at three specific V_b. These applied voltages coincide with the key points highlighted throughout the chapter: at rest (OFF, $V_b = 0$), phase shift region and loss region. The phase shift region is the region where the phase FOM ($FOM^{\Delta\phi}$) is maximum, and the voltage required for this is approximately 7V. The loss region coincides with the maximum value of the loss FOM (FOM^{κ}) and will therefore require a voltage of approximately 3.7 V.

To obtain the modal field at each of these voltages, FEMSIM, an RSoft software tool, was used again. The structure has been simulated (with the non-uniform meshing explained above, Fig. 2.7) at each of the mentioned V_b and the data obtained have been exported to Matlab to facilitate processing and representation. In this way Fig. 2.12 is obtained, which in turn is made up of 3 figures. Each figure (Fig. 2.12 a), b) and c)) is composed of two figures: on the left the representation of the field on the structure in the X and Y axis; on the right the concentration of the field in the E_Y and Y axis.

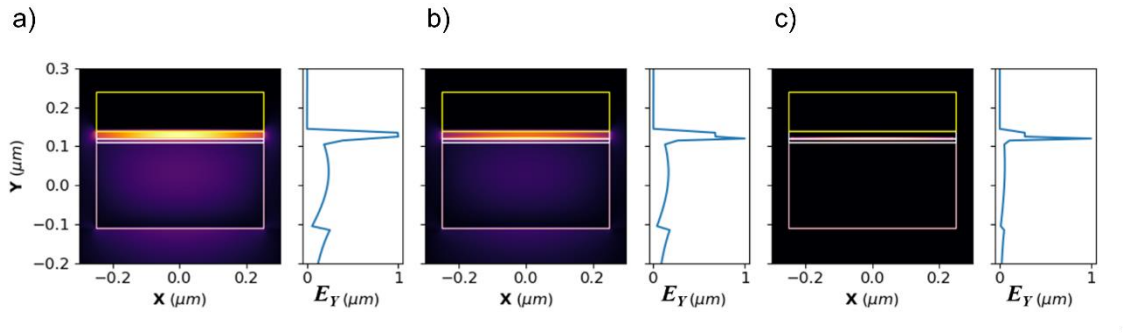

Figure 2.12. Representation of the modal field distribution for the fundamental mode TM. The field shown in the image is the Ey field and the cuts in the structure are made at x = 0. a) shows the field when at rest (OFF, $V_b = 0$ V), b) in the phase shift region ($V_b = 7$ V) and c) in the loss region ($V_b = 3.7$ V).

In Fig. 2.12 a) ($V_b = 0$) it can be seen how the field is predominant in the area where the ITO is located, although in the E_Y field distribution it can be seen that part of the modal field runs through the Si waveguide. Despite the fact that the main concentration is in the desired zone (ITO zone), the field through the Si guide is very significant. Fig. 2.12 b) ($V_b = 7$ V) shows the optimal phase shift performance. It can be seen that the field concentration in the ITO layer is higher than in the previous case, with a small peak appearing in the distribution. This peak coincides with the accumulation layer, as this is where the TCO changes physically occur and therefore where the field must be confined the most. In this case, the field also propagates through the waveguide in a significant way. Fig. 2.12 c) ($V_b = 3.7$ V) shows the modal field distribution for operation in the loss region. In this case the concentration of the EY field is much higher in the accumulation layer causing practically the whole field to be confined in the ITO accumulation region. The distribution in the waveguide in this case can be considered residual. The higher the concentration of the field in the accumulation area, the higher the losses. This is consistent with what is shown globally in Fig. 2.12 since when the structure has more losses the modal field is more confined in the accumulation layer of the ITO.

In conclusion, the modal field is at its maximum level of confinement in the ITO layer (namely in the accumulation layer) when working in the loss region while in the phase shift region and OFF there is confinement in the ITO layer but the propagation through the waveguide is not insignificant.

Chapter 3. Arrayed multilength ITO/Si modulator

3.1 Principle of operation of the arrayed multilength modulator

Transparent conducting oxides (TCOs) have surfaced as remarkable non-linear materials candidates for the design and fabrication of active silicon nanophotonic devices due to its epsilon-near-zero (ENZ) condition at telecom wavelengths [1], as shown in previous sections. Recently, TCOs have shown promise for the development of CMOS-compatible integrated electro-absorption modulators in silicon. Indeed, the permittivity of the TCO can be tuned via carrier accumulation by adjusting the gate voltage in capacitor structure (TCO/Oxide/Metal) such as the one shown previously in Fig. 3.1. Tunning the permittivity near the ENZ resonance results in strong changes on the complex effective index of the hybrid waveguide that can be leveraged to produce amplitude modulation or phase modulation. [40]. However, neither pure- phase nor amplitude modulation can be achieved with a single voltage capacitor as the real and imaginary parts of the permittivity cannot be varied independently. This results in a decreased ability to encode or map any complex number onto the available modulator states. In this context, it is proposed a novel silicon photonic modulator based on a multi-length array of hybrid waveguides loaded with an indium tin oxide (ITO) heterojunction capacitor (Fig. 3.1). The capacitor lengths are selected by following a power of 'b' rule, so that N capacitors enable b^N possible configurations. For example, if 'b' is set to 2 the capacitor would have a total of 2^N possible configurations. The driving voltage of each capacitor can be varied independently. In this way, the proposed arrayed device significantly increases the expressivity of the modulator with respect to a single-length capacitor, generating a quasi-continuous distribution of modulation states on the complex plane.

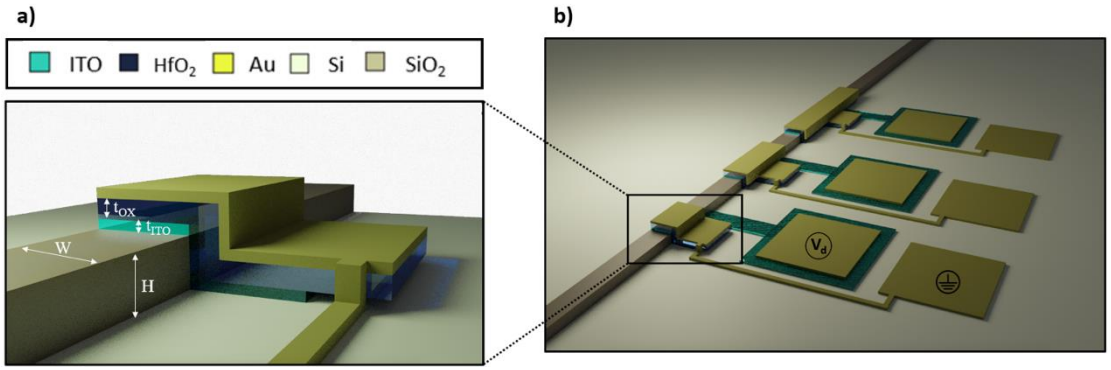

Figure 3.1. Device details for the reconfigurable phase modulator array. a) Zoom-in of the schematics of the ITO capacitor heterojunction phase modulator with device geometry (t_{ITO} = 10 nm; thickness of the HfO_2 gate oxide, t_{ox} = 10 nm; and standard silicon waveguide height, h = 220 nm; and width, w = 500 nm). The ITO contact is used to supply the voltage and the top gold is connected to ground. b) A zoom-out view of the array modulator illustrating the contact placement and general device layout. Capacitor lengths in the example are 1, 2 and 4 microns.

Such device opens up new possibilities on the silicon platform, especially for disruptive applications such as photonic-accelerated neural networks or applications in the GHz regime, like optical phased-arrays, for example. The analysis of the actual performance of the device will be covered in the following section, testing the performance for various lengths and number of modulators following the power of 'b' rule explained above.

3.2 Analysis of the complex-valued modulation performance

In this section, the operation of the multilength device will be analysed. The traditional modulator in which a single voltage is applied, as explained in the previous section, is unable to vary independently the real and imaginary part of the permittivity. This results in just a linear path in the complex plane of possible modulation states. Since the performance is highly dependent on the length of the modulator, so a single basic modulator of 1 μm in length, configured to operate at a wavelength of 1550 nm, has been designed and simulated. Fig. 3.2 has been obtained from this configuration. It can be seen, as theorised, that the possible complex-valued modulation states that can be defined are sparse and cover approximately one quadrant, as far as phase shift (Δϕ) is concerned. The maximum losses are around 30 dB but the biggest problem for the proposed implementations is the low point density.

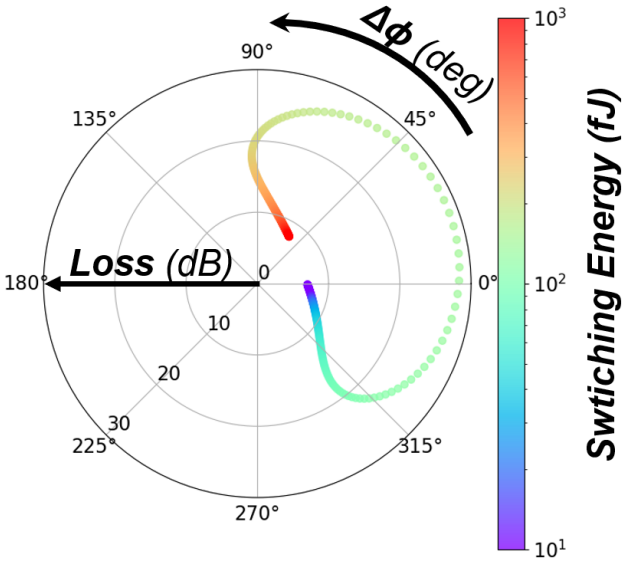

Figure 3.2. Polar representation of the operation of a single modulation (1 μm) according to Losses (dB) and Δϕ (deg)

Once the operation of a single modulator has been analysed, the multilength device will be studied. Prior to the simulation, it is necessary to determine the lengths of the modulators as well as the losses and the phase shift of the set of modulators that make up the device. The lengths of the modulators follow an exponential expression:

$$Modulator\ length = b^n\ \mu m \tag{3.1}$$

Where b is the base of the exponential rule and n is the total number of modulators in the device (N) minus 1. Thus, assuming a base b = 2 and a total of 3 modulators, the length of the first modulator would be 1 μm, the second 2 μm and the third 4 μm. The total length of the device would be the sum of the total length of each of the modulators:

$$Device\ length = \sum_{0}^{N-1} b^n\ \mu m \tag{3.2}$$

The losses and phase shift are determined by the sum of each of the modulators in the device. The losses and phase shift (Δϕ) are obtained for a modulator length of 1 μm, so to obtain these elements for each modulator, they must be multiplied by their actual length. The equations for the losses and Δϕ of the device are the following:

$$Loss = \sum_{n=0}^{\#modulators} b^n Loss^{n=0}\ dB \tag{3.3}$$

$$\Delta\phi = \sum_{n=0}^{\#modulators} b^n \Delta\phi^{n=0}\ deg \tag{3.4}$$

To determine the improvement of the multilength device over the simple modulator, different structures of the multilength device will be simulated in which both the length and the number of modulators will be varied. For the first simulation a base (b) of 2 will be considered and simulated for 2 and 3 modulators. The length of the first modulator is 1 μm, of the second modulator 2 μm and of the third modulator 4 μm. The maps obtained from these simulations can be seen in Fig. 3.3. For the case of 2 modulators (Fig. 3.3 a), the improvement compared to the case of a single modulator lies mainly in a more than considerable increase in the number of combinations but limited by the phase shift and losses that the single modulator presented. For the 3-modulator case (Fig. 3.3 b), the improvement lies in the phase shift obtained. With this design, a wider range of phase shifts is obtained, covering approximately 2 complete quadrants. The maximum losses remain constant.

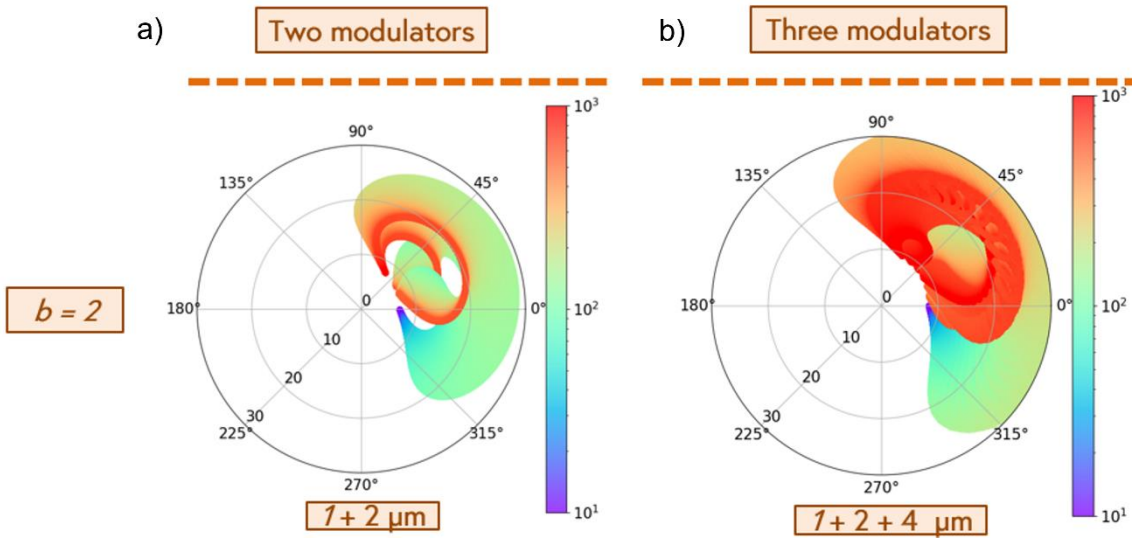

Figure 3.3. Polar representation of the operation of a multilength device (b = 2) according to Losses (dB) and Δϕ (deg). a) Multilength device with 2 modulators. b) Multilength device with 3 modulators

For the second of the simulations, a base (b) of 4 has been considered and simulated for 2 and 3 modulators. The length of the first modulator is 1 μm, of the second modulator 4 μm and of the third modulator 16 μm. The maps obtained from these simulations are shown in Fig. 3.4. For the 2-modulator case (Fig. 3.4 a) the improvement compared to the previous case lies mainly in an

increase of the phase variations thus reaching more than three quadrants. On the other hand, the disadvantage is an increase in the maximum losses. For the 3-modulator case (Fig. 3.4 b) the improvement lies in the phase shift obtained. With this design, a wider range of phase shift is obtained by sweeping all quadrants but losses again increase.

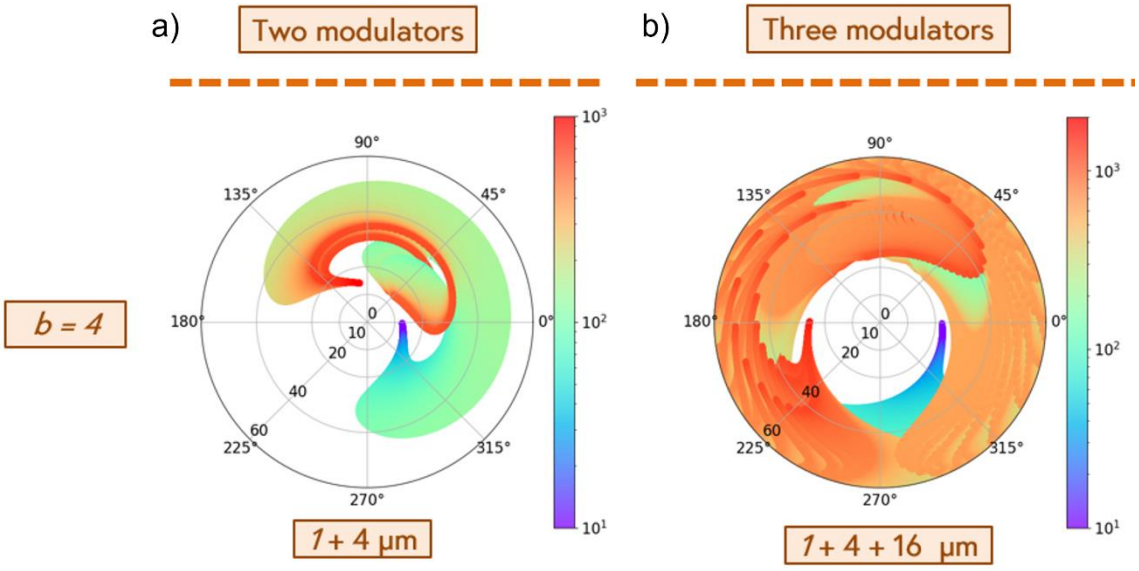

Figure 3.4. Polar representation of the operation of a multilength device (b = 4) according to Losses (dB) and Δϕ (deg). a) Multilength device with 2 modulators. b) Multilength device with 3 modulators

It can be concluded that the number of points in the positioning maps and thus the combinations for the representation of complex numbers increases as a function of the base chosen for the length of the modulators and the number of modulators used in the multilength device. On the negative side, it is shown that as the above parameters increase, the total losses of the device also increase. The best performance in terms of complex number representation is obtained with a base (b) of 4 and 3 modulators, since all the options in terms of phase shift are swept, but it is the configuration with the highest losses.

Such a device presents great interest for novel technological applications such as photonic neural networks. Indeed, large matrix multiplications with complex numbers could be run under a hardware loaded with multi-length arrays such as this one.

Chapter 4. Route towards improved performance

4.1 Replacing ITO by other TCOs

This section aims to improve the initially designed capacitor by replacing the ITO layer with other TCOs. Here the concept of mobility gains importance. Mobility is a unique characteristic of each material and will vary when using different TCOs. Materials with low mobility have limited usefulness due to their high losses. High mobility implies low losses, so it is intended to work with high mobility materials whenever possible. Up to this point, the ITO was being used whose mobility (μ) is $20 \cdot 10^{-4}\, m^2 \cdot V^{-1} \cdot s^{-1}$, as specified in section 2.2 above. This mobility, compared to that of other TCOs, is not very high, so the use of CdO as a supplementary material is proposed. The CdO, specifically CdO:Dy (CdO doped with Dysprosium) that will be used, has a μ of $150 \cdot 10^{-4}\, m^2 \cdot V^{-1} \cdot s^{-1}$ [41] (or higher depending on its carrier concentration), a value considerably higher than that of ITO and with which it is intended to obtain better results.

The same optimal structure will be used as with the ITO modulator, i.e., the oxide (HfO_2) will have a thickness of 10 nm. The CdO layer will also be set at 10 nm, of which 1 nm will be allocated to the accumulation layer. Fig. 4.1 shows the structure of the hybrid Si/CdO modulator. For the study, the same steps will be performed as for the ITO except for the optimisation of the oxide thickness, which, as mentioned above, is set at 10 nm in order to compare the performance of the devices with a single structure.

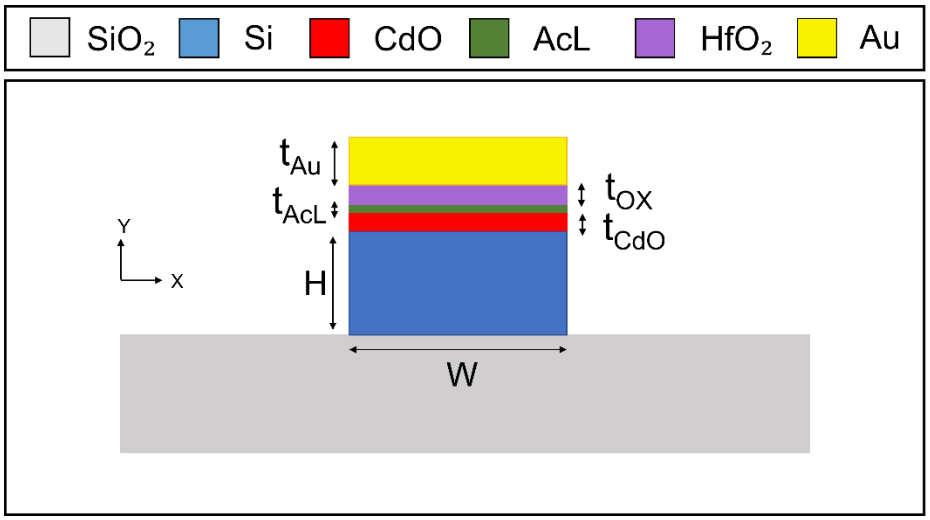

Figure 4.1. Structure of the hybrid Si/CdO capacitor with the accumulation layer.

4.1.1 Modelling of the CdO permittivity near the ENZ

In this subsection, the behaviour of CdO near the ENZ region will be modelled. The same model (Drude model) and formulae will be used as in the case of ITO. The difference will lie in the unique parameters of each material. To determine the permittivity, Formula 2.1 is used where, for CdO:Dy, it is set: $\varepsilon_\infty = 5.6$ [41]; $m_0 = 0.16 \cdot m_e$ [41]. Taking into account that the mobility (μ) was $150 \cdot 10^{-4}\, m^2 \cdot V^{-1} \cdot s^{-1}$ and applying it in Formula 2.2, the complex permittivity as a function of CdO carrier concentration (N_{CdO}) is obtained in Matlab. This is set as a vector between $0.1 \cdot 10^{21}$ and $1 \cdot 10^{21}\, cm^{-3}$, typical values for N_{CdO}. From the permittivity, the complex refractive index of CdO is obtained, also as a function of N_{CdO}. In this way, a first approximation of the behaviour of CdO and its change in behaviour as a function of carrier concentration is obtained. Fig. 4.2 shows the three behaviours experienced by the material, behaving as a dielectric for N_{CdO} lower than $4.1 \cdot 10^{20}\, cm^{-3}$ (real part higher than the imaginary part of the complex

index), as a metal for higher concentrations (real part lower than the imaginary part of the complex index) and as an ENZ element at an N_{CdO} around $4.1 \cdot 10^{20}\ cm^{-3}$ (crossover between real and imaginary part, same value at 1550 nm wavelength).

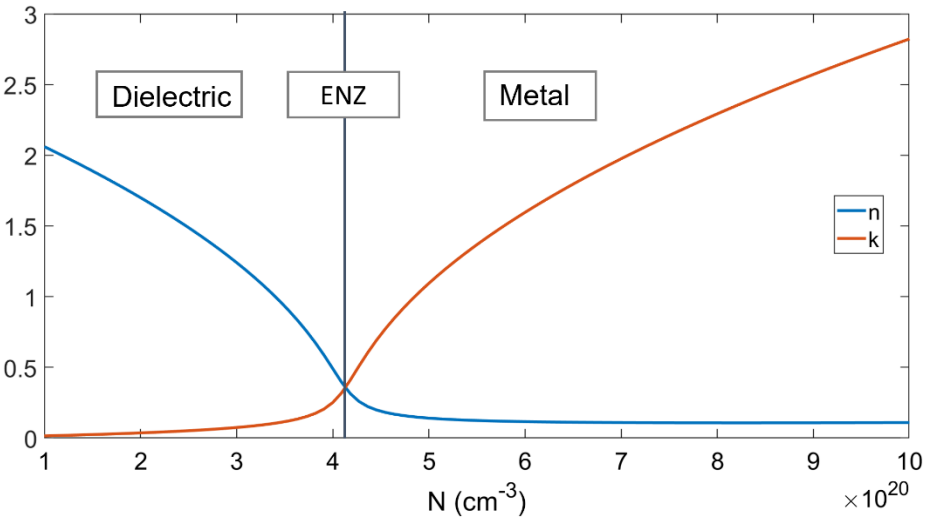

Figure 4.2. Complex index vs carrier concentration for CdO.

This point ($N_{CdO} \simeq 4.1 \cdot 10^{20}\ cm^{-3}$) is where the real part of the complex permittivity crosses through zero (Fig. 4.3), demonstrating the ENZ criteria.

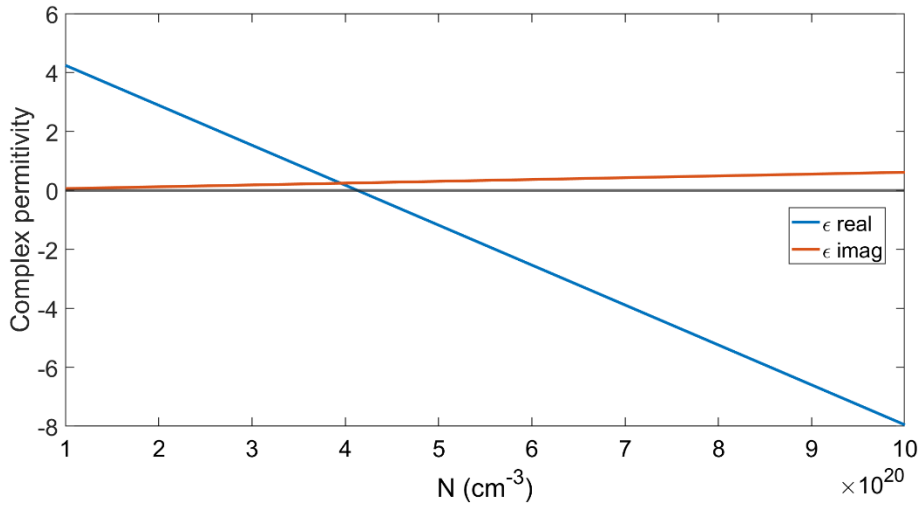

Figure 4.3. Complex permittivity vs carrier concentration for CdO.

To obtain the complex index as a function of bias voltage, the above Formulas 2.3 and 2.4 are applied, which are implemented on the full structure in Fig. 4.1. The effect and creation of the accumulation layer is identical to the ITO case as the oxide in the structure is the same but the N_0 varies in this case. To the CdO the N_0 is set to $8 \cdot 10^{26}\ m^3$ [41]. This results in Fig. 4.4. It can be seen that in the case of the hybrid Si/CdO modulator, the bias voltage required to operate in the ENZ region is approximately 2.4 V. The analysis of the overall performance of the device will be studied in the next subsections.

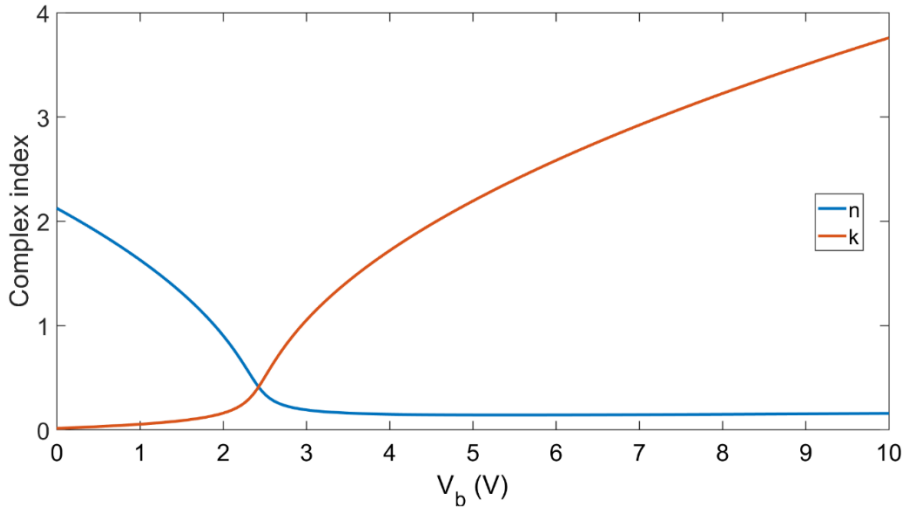

Figure 4.4. Complex index vs bias voltage (V_b).

4.1.2 Estimation of the complex effective index

As in the previous case with ITO, once the behaviour of CdO has been determined, it is essential to study the operation of the complete device. For this purpose, FEMSIM will be used again in the same configuration as in the previous case. The meshing will be non-uniform and identical to the one already used (Fig. 2.7). In this way, the complex effective index of the structure is obtained in FEMSIM. These data are exported to Matlab where they are processed to obtain Fig. 4.5. This figure shows the evolution of the complex effective index as a function of the bias voltage (V_b) applied to the device. It can be seen that the variations in the index are centred in the range between 1 and 4 V for both the real and imaginary parts. For an applied voltage outside this range the variations in the complex effective index are zero or almost imperceptible.

The changes in the CdO structure are very abrupt and fast which indicates that a small change in voltage varies the index a lot. As with ITO, the ENZ region of the device matches that of the material. The structure shows maximum losses when the imaginary part of the complex effective index of the structure (κ_{eff}) is maximum. This happens at a voltage around 2.4 V, just like the CdO layer studied in the previous subsection. The structure at 2.4 V shows a complex index equal to 2.828 + 0.390 j.

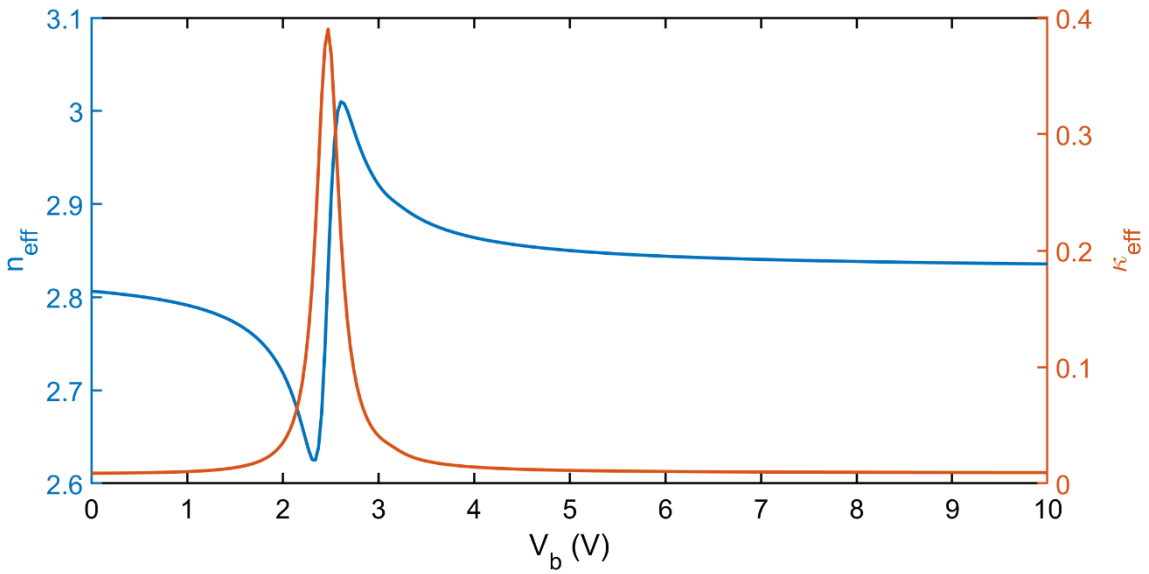

Figure 4.5. Evolution of the complex effective index of the CdO structure versus bias voltage (V_b)

An important feature of this structure can also be seen in Fig. 4.5. This feature is the low losses available to the device when it is at rest ($V_b = 0$). When no voltage is applied to the structure it has a $\kappa_{eff} = 0.009$. This value is very low and more than adequate for the actual implementation of the modulator. This is due to the possibility of modulating both amplitude and phase when required but having very low losses when it is not necessary to modulate. The performance of the device will be discussed in more detail in the following subsection.

4.1.3 Analysis of FOMs, operation voltages and energy consumption

In this subsection, the main features of the device will be developed. To do this, the FOMs to be used will be obtained. A phase FOM ($FOM^{\Delta\phi}$, Formula 2.5) and a loss FOM (FOM^{κ}, Formula 2.7) will be used as in chapter 2. The aim is to obtain the maximum values of both FOMs as a function of the applied bias voltage and the energy consumption. With the formulas of the figures of merit already presented, the graphs as a function of V_b can be obtained without any problem. The representation as a function of the energy consumed requires the relation between V_b and energy. For this purpose, the Formulas 2.8 and 2.9 are used again. Since the structure is the same as for the ITO and the different capacitor materials are also the same, it is not necessary to go into detail on the implementation of these equations as it was explained in chapter 2.

Thus, Fig. 4.6 is obtained, on which the different optimum performances of the device will be analysed.

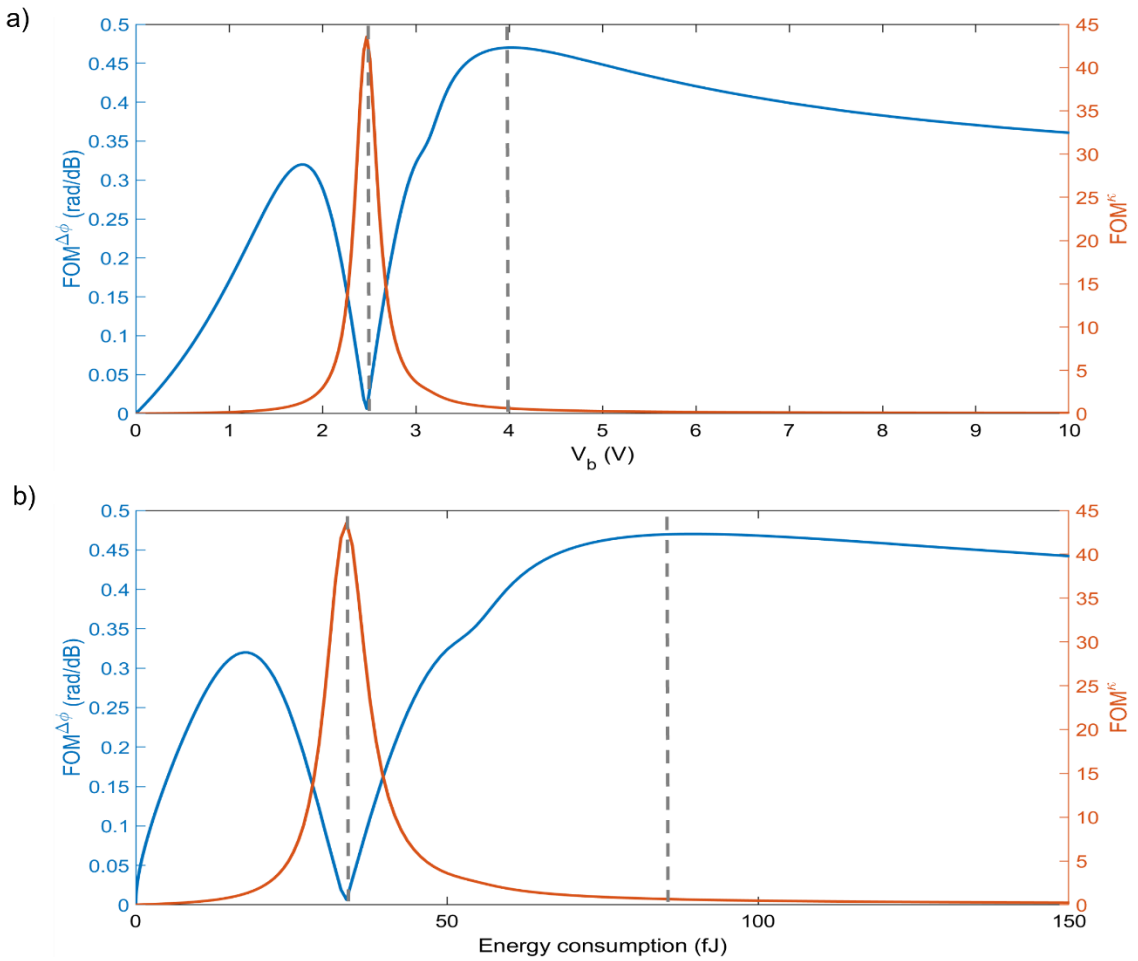

Figure 4.6. Plot of the two FOMs defined as a function of bias voltage (a) and energy consumption (b)

For optimal operation for losses, a bias voltage of approximately 2.4 V must be applied, thus obtaining a power consumption of 45 fJ. On the other hand, to work when the $FOM^{\Delta\phi}$ is maximum, it is necessary to apply 4 V to the structure. At this point, 87 fJ are consumed.

It is interesting to note that the maximum values reached by the FOMs in this case (CdO) are much higher than the values obtained with ITO, in addition to the fact that the voltages required and, therefore, the energy consumed are also lower in the case of CdO. A more exhaustive comparison will be carried out in the following section, where a summary of both designs will be made.

4.2 Summary of final designs

In this section we will summarise both the basic structure initially proposed, in which the ITO is used as the TCO, and the proposal for improvement with the CdO. For this purpose, Table 4.1 and Table 4.2 have been drawn up, in which the most decisive aspects analysed throughout this work are included. Both tables are separated into two parts: the properties of the material applied in each structure and the performance metrics of the modulator. The performance metrics have been analysed in the three key operating regions: OFF ($V_b = 0$), phase shift region ($V_b = V_{\Delta\phi}$) and loss region ($V_b = V_\kappa$).

ITO

Material properties	ε_∞	3.66		
	m_0	$0.49 \cdot m_e$		
	μ	$20 \cdot 10^{-4}\ m^2 \cdot V^{-1} \cdot s^{-1}$		
		$V_{OFF}\ (0\ V)$	$V_{\Delta\phi}\ (7\ V)$	$V_\kappa\ (3.7\ V)$
Performance metrics	$\Delta\phi\ (\mathrm{rad}/\mu m)$	–	0.25	0.06
	$Loss\ (\mathrm{dB}/\mu m)$	1.88	2.44	6.43
	$FOM^{\Delta\phi}\ (rad/dB)$	–	0.13	0.02
	FOM^{κ}	–	0.36	3.09
	$E_s\ (fJ/\mu m)$	–	270	75

Table 4.1. Summary of ITO final design where the material properties and key performance metrics of the device are listed.

The mobility (μ) in ITO is relatively low compared to other TCOs, so the performance of the structure is not as good as could be achieved with other materials. Other materials such as CdO (Table 4.2) have a much higher μ, namely 7.5 times higher. Comparing the performance metrics of both structures, it can be seen that in most cases the device with CdO performs better. As for the phase shift per micron [Δϕ (rad/μm)], the phase shift obtained when no voltage is applied is zero in both cases. When $V_{\Delta\phi}$ is applied, the performance with CdO is identical to the case with ITO. On the other hand, when V_κ is applied (voltage where losses and no phase shift are desired), ITO has a phase shift of 0.06 rad/μm while in CdO it is 0.22 rad/μm, which might be beneficial depending on the application.

In terms of losses (dB/μm) when no voltage is applied the CdO performs much better than the ITO as it has much lower losses. The same is true when $V_{\Delta\phi}$ is applied. On the other hand, when the optimum voltage for the losses is applied, the losses are much higher in the case of CdO, again demonstrating the better performance of CdO. In the case of the FOMs they are similar. The

FOM$^{\Delta\phi}$, when the phase shift voltage is applied, is 3 times higher in the case of CdO. The FOM$^{\kappa}$ presents a value more than 10 times higher for the CdO case when the loss voltage is applied. Finally, the energy consumed is much higher in the case of ITO for both $V_{\Delta\phi}$ and V_{κ} (for the initial case, as no voltage is applied, there is no energy consumption), so again the structure with CdO is more suitable as low energy consumption is desired.

CdO

Material properties	ε_∞	5.60		
	m_0	$0.16 \cdot m_e$		
	μ	$150 \cdot 10^{-4}\ m^2 \cdot V^{-1} \cdot s^{-1}$		
		$V_{OFF}\ (0\ V)$	$V_{\Delta\phi}\ (4\ V)$	$V_{\kappa}\ (2.4\ V)$
Performance metrics	$\Delta\phi$ (rad/μm)	–	0.25	0.09
	$Loss$ (dB/μm)	0.31	0.50	13.74
	$FOM^{\Delta\phi}\ (rad/dB)$	–	0.47	0.01
	FOM^{κ}	–	0.60	43.56
	$E_s\ (fJ/\mu m)$	–	87	45

Table 4.2. Summary of CdO final design where the material properties and key performance metrics of the device are listed.

In conclusion, the CdO device performs better in most scenarios. This is due to its higher mobility which, as already argued above, is crucial for a better performance of this type of device. Taking only this into account, the final device would have the CdO as TCO. Although it has better performance, the aim of this work is to design and develop a structure whose components can be used experimentally at the research institute where the work is being carried out (NTC, Nanophotonics Technology Center). Since CdO is toxic and its use is regulated in Europe, ITO, which is available at the NTC, will be used for the following chapter on fabrication and measurements.

Finally, the oxide used will be discussed. For this design, HfO_2 has been used. This oxide has been considered from the beginning and has not been proposed to be modified. This is because other possible insulators such as SiO_2 have a much lower dielectric constant. Thus, SiO_2 cannot be used as it would require a bias voltage of approximately 30 V and the breakdown point of this material is lower than this voltage (approximately 25 V) [42]. In other words, the voltage required to produce the changes would be higher than the voltage supported by the structure and the device would burn out. HfO_2 has therefore been chosen as the oxide used to realise the MOS-like capacitor.

Due to the fact that this is an amplitude and phase modulator, it is essential to analyse both the phase shift ($\Delta\phi$) and the losses (α) not only in the areas of interest represented in Table 4.1 and Table 4.2, but also in the whole range of applicable voltages. Fig. 4.7 shows this behaviour for the ITO structure, where the evolution of $\Delta\phi$ and α as a function of the applied V_b can be appreciated. As can be seen, when 3.7 V (V_{κ}) is applied, the losses are the maximum. In contrast, the maximum phase shift does not occur at 7 V, the voltage at which the $FOM_{\Delta\phi}$ was maximised. This is due to the effect of losses. With the $FOM_{\Delta\phi}$, the aim was to obtain a large phase shift but at low losses. When $\Delta\phi$ is maximum (around 4.7 V) the system has considerable losses (4.5 dB/μm) so the $FOM_{\Delta\phi}$ does not reach its maximum.

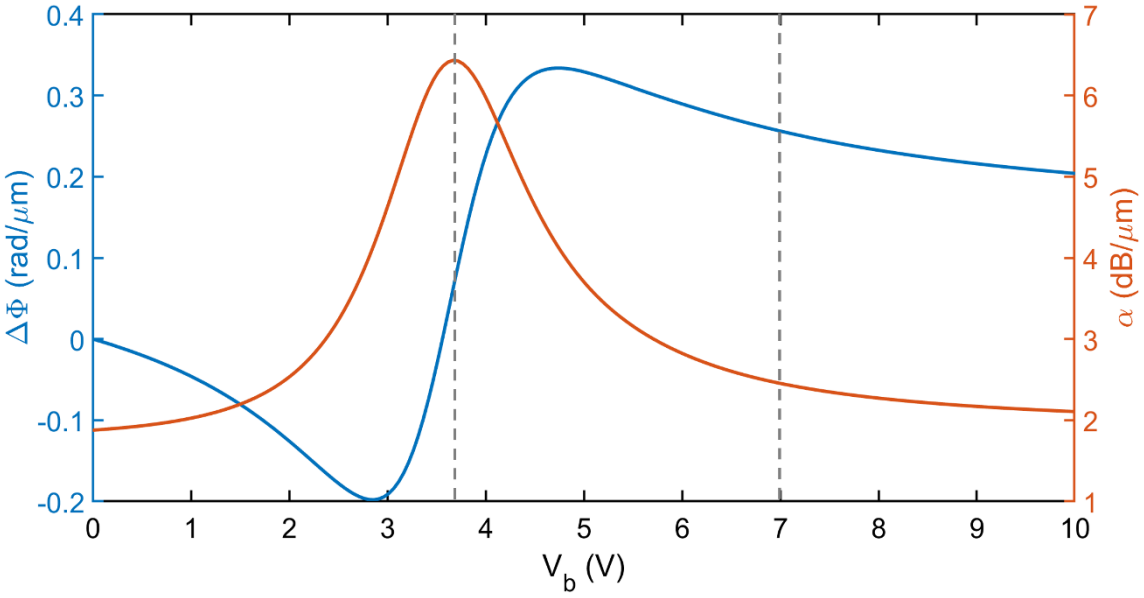

Figure 4.7. Evolution of the phase shift (Δϕ) and losses (α) of the ITO modulator as a function of the bias voltage (V_b).

Fig. 4.8 is analogous to the previous one but for the CdO case. As in the previous case, the maximum losses of the device (α) coincide with the Vκ (2.4 V) given by the FOMκ. The main difference between the two materials is that the resonances in CdO are narrower and more pronounced than in ITO.

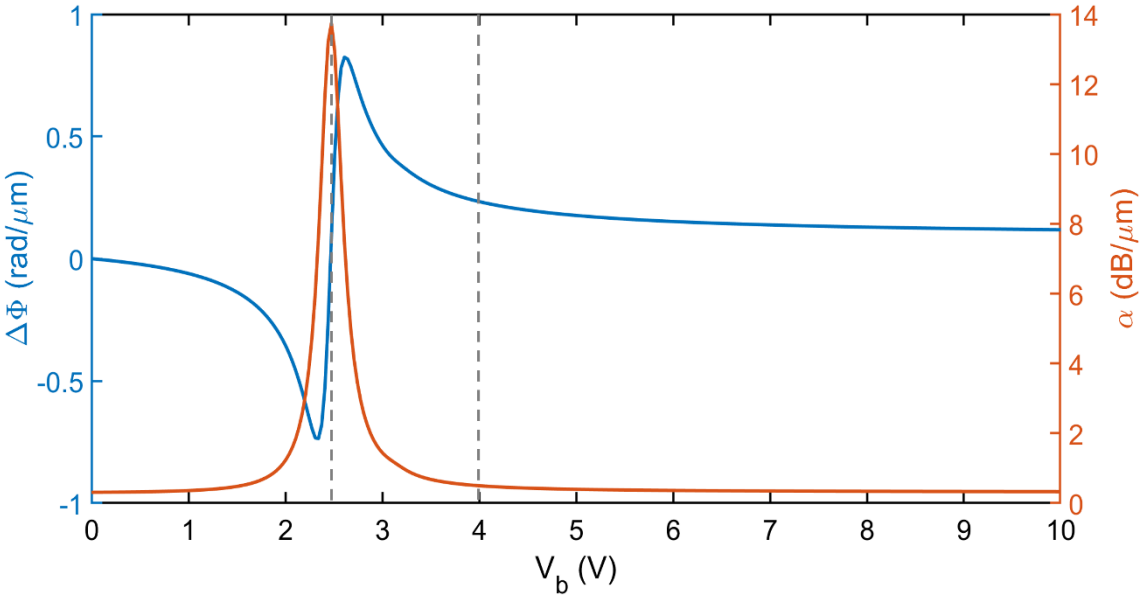

Figure 4.8. Evolution of the phase shift (Δϕ) and losses (α) of the CdO modulator as a function of the bias voltage (V_b).

In this way, the most important aspects of the modulator in both ITO and CdO have been compiled, as well as its performance in terms of Δϕ and κ.

Chapter 5. Fabrication and experimental results

5.1 Description of the experiment

The aim of this experimental part is to extract the TM mode losses at 1550 nm from a hybrid ITO-Si waveguide and to introduce the nanofabrication technique used in the experimental realization of such devices. This experiment will discard the capacitor structure completely and will be solely focused on the tuning of the carrier concentration of an ITO thin film deposited on of a silicon waveguide. This design choice was done as a first step towards the development of the final capacitor structure, with the aim of optimizing the position of the ENZ wavelength of the ITO. This experiment has been carried out at the Nanophotonics Technology Center (NTC), a research institute linked to the UPV, in collaboration to an external research group based on the School of Science and Technology, based on the Nottingham Trent University (United Kingdom).

An ITO/Si waveguide was designed to characterize the TM mode losses. In our experiment, the modal transmission will be measured after the light propagation in a standard Si waveguide and then compared with an ITO-loaded piece of hybrid waveguide. Both structures can be seen in Fig. 5.1. The first one (Fig. 5.1 a) is just the standard silicon (Si) waveguide (500 x 220 nm) on a SiO_2 substrate. The second structure (Fig. 5.1 b) is also a standard silicon on insulator (SOI) waveguide on which a 50 nm ITO layer is grown on top. By contrasting the measurements on the structures, it is possible to obtain the losses provided by the ITO layer to the device.

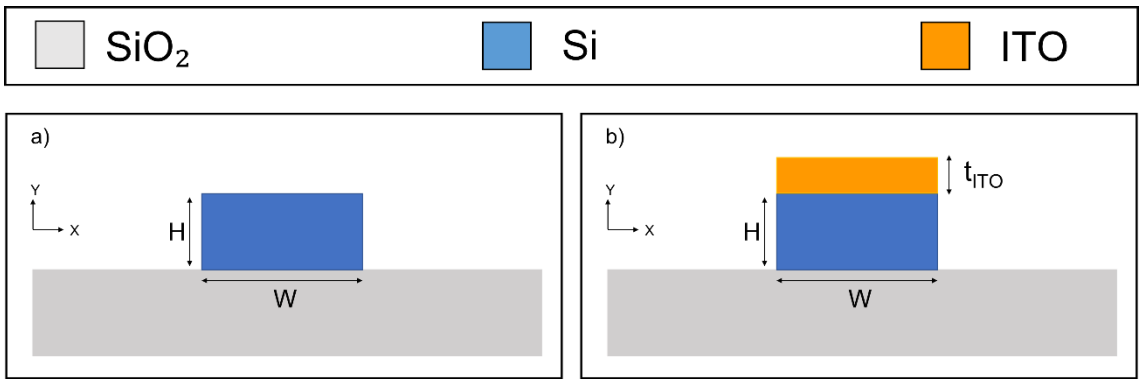

Figure 5.1. Structures that will be used throughout the experiment. a) Shows the base structure, a standard Si waveguide above SiO2. b) Shows the structure of a) but with the addition of a 50 nm ITO layer above the waveguide.

The choice of ITO thickness is determined by taking into account the fabrication limitations of the material. Throughout the project, the ITO layer was set at 10 nm, but for this experiment, a safety margin of 50 nm was chosen in order to make the ITO surface more homogeneous and to smooth-out the possible roughness.

The following section will explain in more detail the fabrication process of the structures explained here.

5.2 Description of fabrication process

The fabrication process is divided into two main parts: the fabrication of the waveguide (necessary for both structures, Fig. 5.1 a and Fig. 5.1 b) and the deposition of the ITO layer on the waveguide (only necessary for the second structure, Fig. 5.1 b).

First, the fabrication of the waveguide will be explained. The starting point is initially a substrate of SiO_2 with a thin 220 nm film of Si on top of it. The SiO_2 forms the base and should therefore remains intact throughout the process. On the other hand, it is on the Si layer that the waveguide is going to be inscribed. Thus, the excess Si must be removed to form the waveguide. To do this, electron-beam lithography (e-beam or EBL) is used, which consists of focusing a beam of electrons on a protective working surface (resist) to create patterns or shapes that are then transferred to the substrate. At the NTC, JBX-8100FS Jeol ultrafine e-beam machine is used for lithography. Prior to this step, it is necessary to apply a layer of resist on the substrate, which will be collect the e-beam dosis. There are two types of resists, positive and negative.

Positive resists are those in which, by using the e-beam, the areas that will later be eliminated are exposed. This is a reverse design. Negative resists work the other way round. With the e-beam, the areas of the final design that are not intended to be removed are exposed, forcing the electron beam to focus on the desired design. A negative resist has been used in the fabrication of the waveguide, so the e-beam must be focused on the waveguide.

Once e-beam has generated the patterns, the only thing left to do is to eliminate the unexposed resist areas, those where the electron beam has not been focused. For this purpose, a chemical attack with different gases is carried out, which eliminates the unexposed resist and the Si underneath these areas of the resist. Once the attack is finished, the final step is to remove this resist. This process is known as lift-off and consists of immersing the substrate with the resist in acetone for 24 hours. The result of this cleaning is the desired final structure, in this case the Si waveguide on the SiO_2 base.

Fig. 5.2 shows a diagram summarising the steps explained:

(1) An initial block composed of Si and SiO_2 is available.
(2) A thin layer of negative resist (HSQ) is applied to the starting block.
(3) The resist is sent to e-beam on the area that is not intended to be removed. The properties of the resist change and make it gas resistant.
(4) Unexposed sections of the resist are removed (developing).
(5) The structure is etched to remove the unwanted areas.
(6) The sample undergoes lift-off and results in the desired final structure.

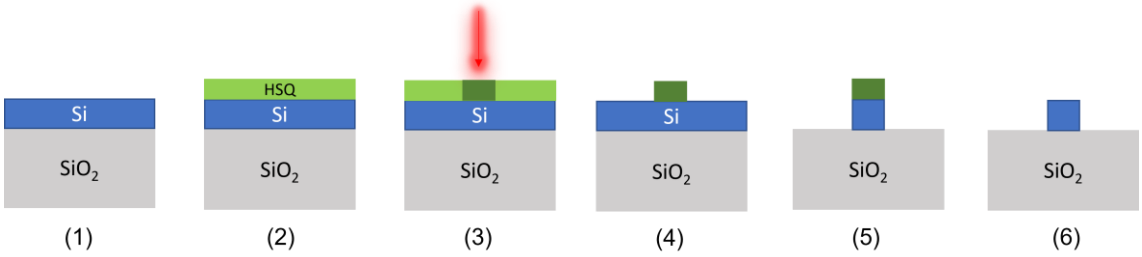

Figure 5.2. Fabrication process of a Si waveguide

This explains the first part of the fabrication, which will produce the complete structure of Fig. 5.1 a and the base of Fig. 5.1 b. The second part of the fabrication is the deposition of the ITO layer on the Si waveguide, and this will only be necessary for the structure in Fig. 5.1 b. This process is explained below.

The first part of the process is similar to the previous one since it is necessary to apply a resist on the waveguide and then subject it to e-beam. In this case the resist used is a positive resist. As it is positive, only the area that is intended to be eliminated during development, in this case the waveguide, will be sent to the e-beam. Once the e-beam has been carried out, development takes place, leaving the waveguide uncovered.

The next step is where the ITO is deposited on the sample. In this case, RF-sputtering has been used. This technique consists of using ionised gas molecules to evaporate the ITO, so the target material molecules are deposited on the desired sample. Once the sputtering is finished, it is only necessary to remove the remaining resist and the ITO on top of it. For this purpose, the lift-off is used again to obtain the Si waveguide with the ITO layer on top of it.

Fig. 5.3 shows a diagram as a summary of the steps explained:

(1) The Si waveguide obtained in the first part of the fabrication is available.
(2) A layer of positive resist (PMMA) is applied.
(3) The resist is e-beamed over the area to be removed. The properties of the resist change and make it soluble for development.
(4) The exposed areas of the resist are removed (developing).
(5) Sputtering is applied, and ITO is deposited on the entire sample.
(6) The sample is lift-off and the Si waveguide with the ITO layer on top is obtained.

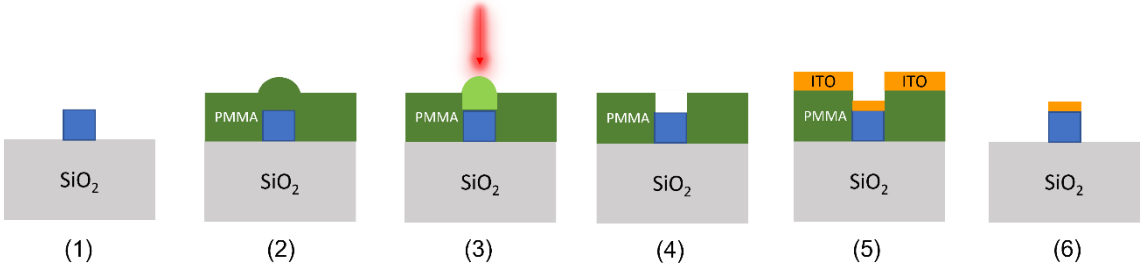

Figure 5.3. Process by which a layer of ITO is deposited on the SI waveguide.

In order to optimize the ENZ wavelength position in the third telecom band (1550 nm), an additional annealing post-processing step needs to be conducted on the ITO layer. Indeed, in the formed ITO films, oxygen vacancies dominate the conduction mechanism of ITO film by contributing two free electrons (i.e., contributes to the carrier density of the film) [43]. Thus, post-deposition annealing is an effective way to control the number of oxygen vacancies and, therefore, to reduce the number of free electrons, decreasing the carrier density.

In this research work the annealing of our samples was performed via a technique known as Reactive Laser Annealing (ReLA) [44], which was applied by our collaborators (Tomas H. Howe from Nottingham Trent University). The changes produced by ReLA were studied by ellipsometry measurements, which show that the ENZ wavelength was tuned around 1550 nm.

In this way the fabrication of the samples is completed.

5.3 Design of the mask file

This section aims to explain how the mask for fabrication has been designed. To do this, a mask has been designed in such a way that it can be applied to the processes described above in the fabrication (specifically in the EBL) in order to obtain the test samples to be used. Graphic Design System (GDS) files are typically used to describe the mask to the EBL machine. These files are the most commonly used to transmit information about the design of integrated circuits nowadays. To make the GDS, the free software KLayout has been used in this project. The use of this tool is very extended and allows the visualisation and creation of GDS files.

In order to design the device mask in KLayout, an optimized library containing the necessary structures was imported from Matlab. Such library was developed in the context of the Photonic Integrated Devices research group of the NTC, and it is highly optimized to work with the

nanofabrication equipment of the NTC. The structures used for the design were gratings, straight waveguides, waveguide bends and rectangles to implement the ITO layer. With all these blocks, the GDS file that can be seen in Fig. 5.4 is designed. It can be seen how the same geometry was utilized to define 5 different devices.

Each of these devices has gratings optimised to work with TM polarisation at wavelengths of around 1550 nm. These gratings are the elements located at the ends of the devices. Furthermore, as can be seen in Fig. 5.4, with the exception of the first device (reference device without ITO), all the waveguides have a patch of ITO of different lengths. From top to bottom, the ITO layer lengths are 5, 7.5, 10 and 12.5 µm respectively. All waveguides have the standard size (500 x 220 nm).

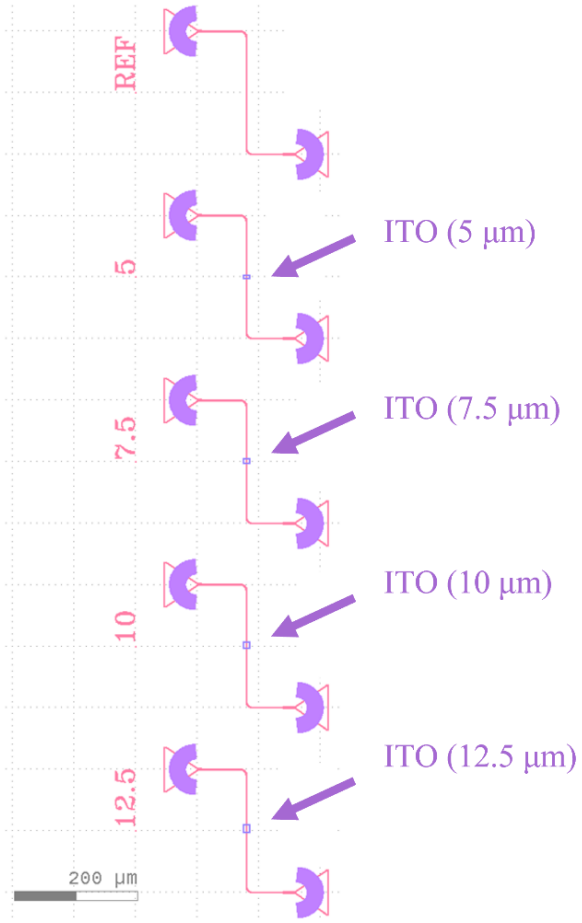

Figure 5.4. Design of the mask in the GDS file.

5.4 Analysis of fabricated sample

The fabrication of the sample and the mask design have already been explained so the process for obtaining the sample is complete. The sample has been fabricated at NTC and sent to Nottingham Trent University for ITO tuning in the ENZ region at 1550 nm. The first step after receiving the sample back is to do a first check to make sure that everything has gone correctly. To do this, the fabrication sample will be observed in detail with an optical microscope. Specifically, a Zeiss microscope, model Axiolab 5, was used. Fig. 5.5 shows the general view from the microscope of two of the structures, namely the silicon waveguide (Fig. 5.5 a) and the silicon waveguide with the 12.5 µm long ITO patch (Fig. 5.5 b).

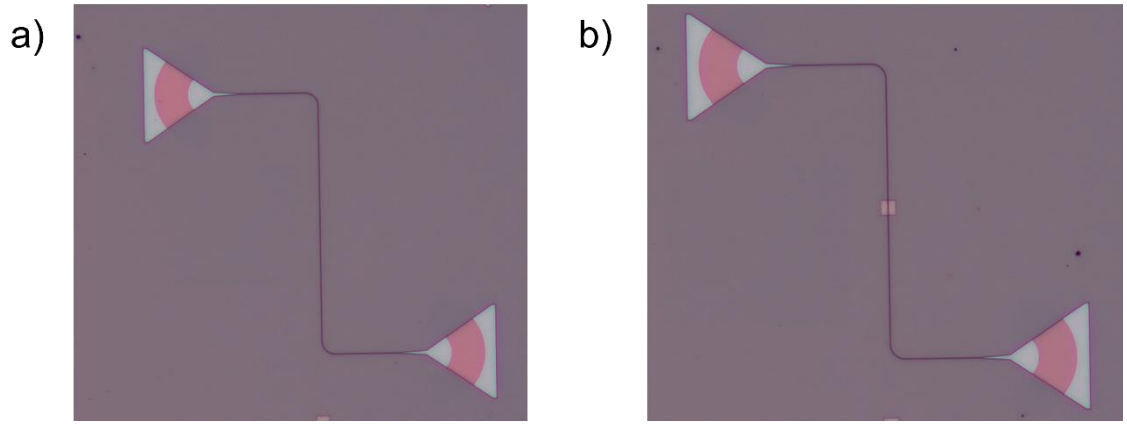

Figure 5.5. Optical microscope view of the sample structures. a) Silicon waveguide. b) Silicon waveguide with an ITO layer of 12.5 µm length.

For devices with ITO, the condition of the material is essential, so the area has been zoomed in (see Fig. 5.6, where a general view of the structure and an expanded view of the ITO layer can be seen). In this way, all structures are checked to ensure that they are in good condition and suitable for measurement.

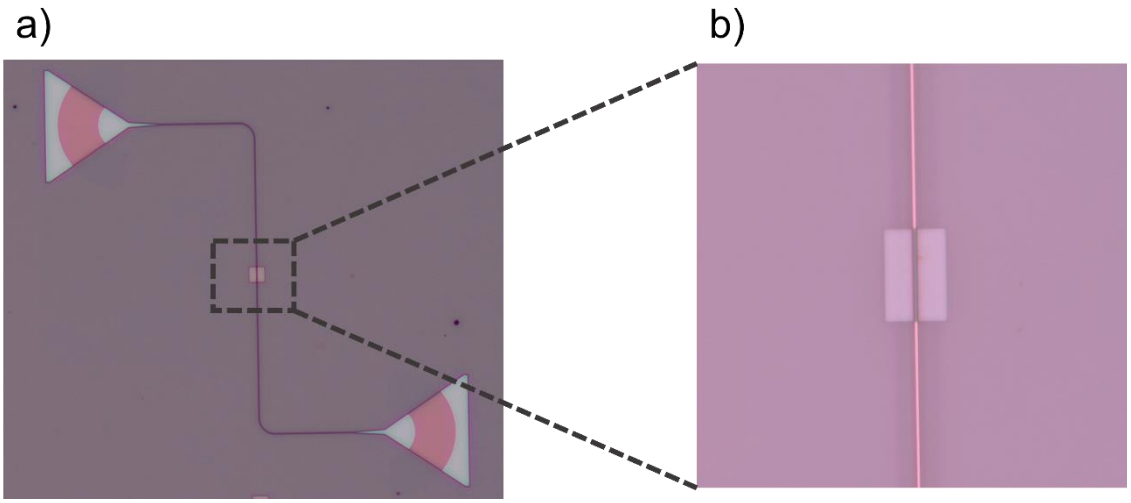

Figure 5.6. a) Silicon waveguide with a 12.5 um long ITO layer. b) Zoom of the ITO layer.

5.5 Description of experimental set-up

The schematic of the set-up used for the experimental measurements is shown in Fig. 5.7. As shown, a laser is used which emits a continuous wave (CW) signal which in the current case is configured to inject an electrical power of 1 mW (0 dBm). The laser allows the wavelength of the signal to be varied between 1540 and 1580 nm. This CW signal is sent through the polarisation controller. This is used to manually select the polarisation of the light passing through it. It consists of three rotational plates which will be placed in this experiment so that the polarisation of the signal is TM since the sample works with this polarisation.

To check that the polarisation set is correct, it can be checked visually on the Power Meter (PM), which is in charge of measuring the output power of the Device Under Test (DUT). This Power

Meter has a photodiode which converts the light into electrical power to be displayed on the PM. A real image of the elements mentioned so far can be seen in Fig. 5.8.

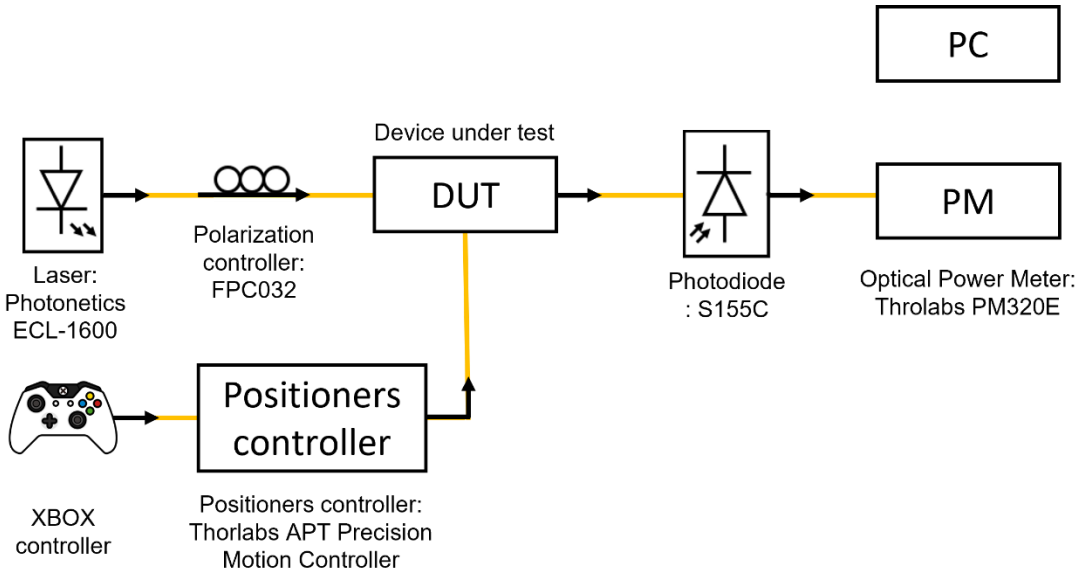

Figure 5.7. Schematic of the set-up used in the experiment.

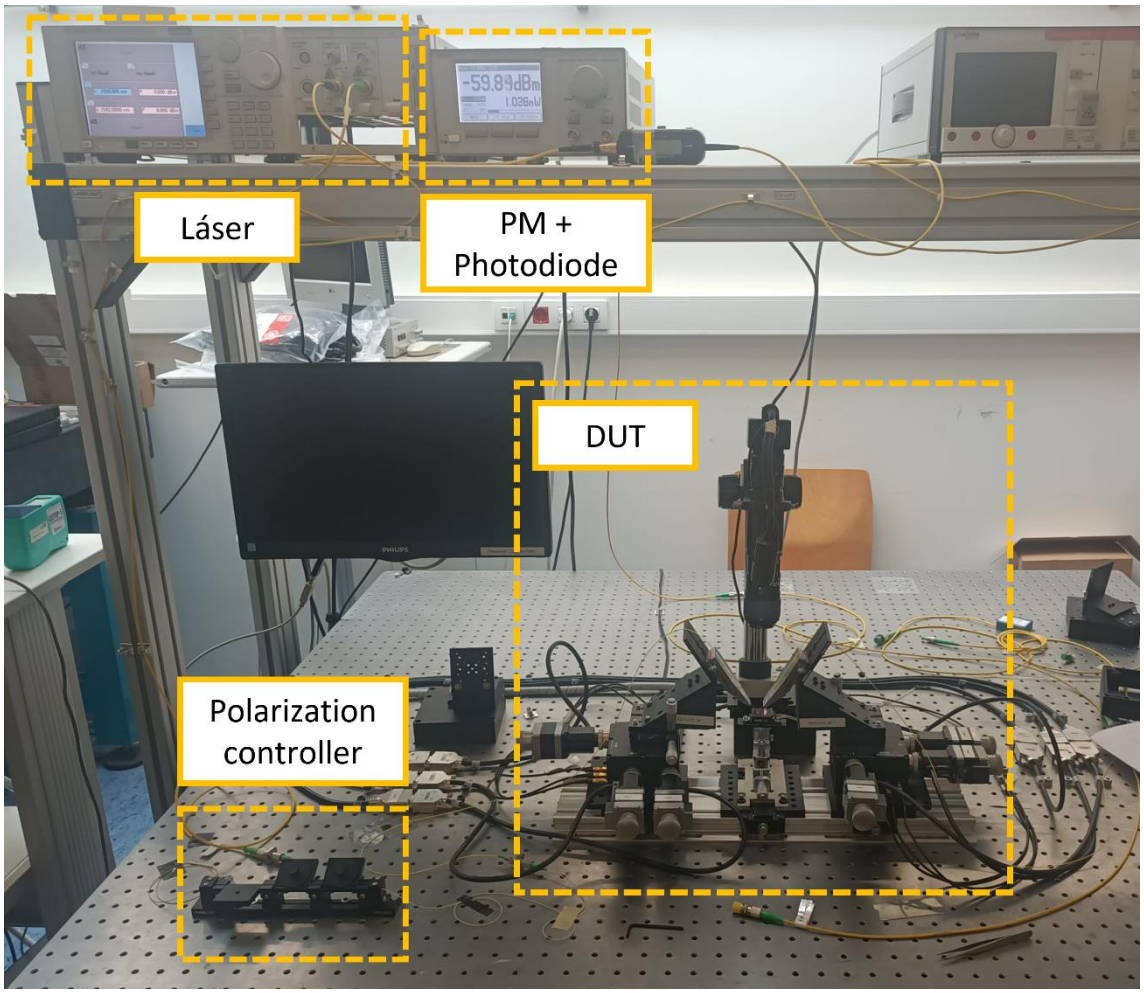

Figure 5.8. Image of the set-up.

The position of the DUT is critical so it must be fixed in the holder. To achieve this, the holder has a vacuum suction function. The light enters and exits the sample via two optical fibres. The position of the fibres in relation to the sample is critical as the fibres must be aligned with the grating of the structures. For this purpose, the supports that hold the optical fibres have a positioner. Each fibre has one and they are used to move the fibres in the X, Y and Z axes to adjust them to the desired position. In addition, there is a camera and a light connected to a monitor to ensure the correct positioning of the guides. The above mentioned elements can be seen in Fig. 5.9.

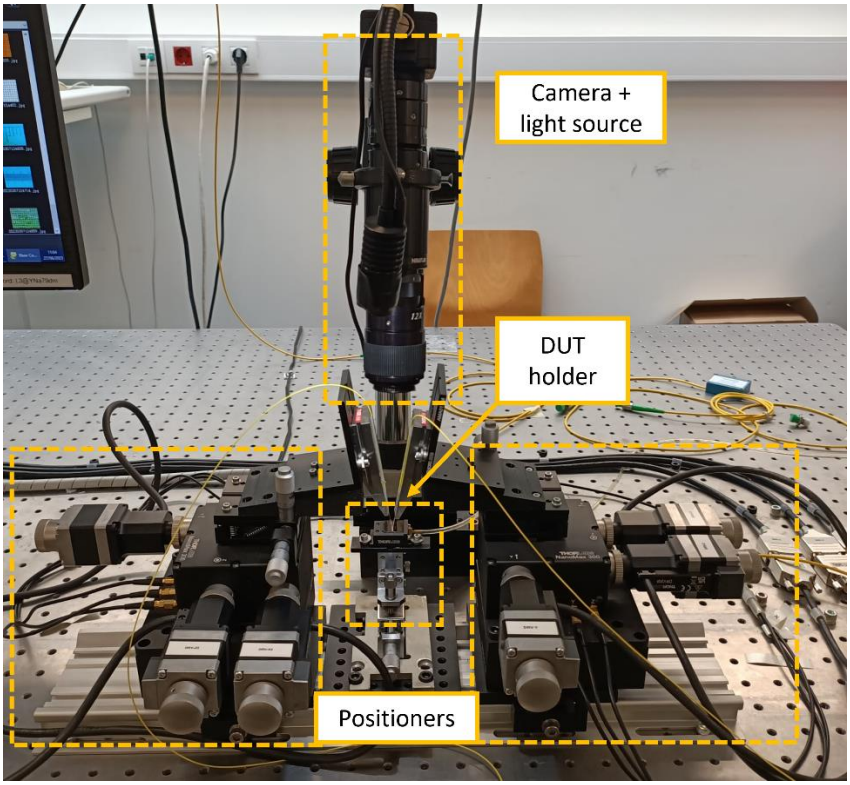

Figure 5.9. Image of the DUT holder, camera and positioners.

This is an automatic set-up whereby the positioners mentioned above are controlled by a series of motion motors which in turn are controlled by a program implemented in the laboratory computer. The program is designed to be run with an XBOX controller. With the controller you have full control over the three axes of the platforms of each of the fibre optics. In other words, the controller executes a program in the computer which sends the movement orders to the motor that moves the positioners. All these elements can be seen in Fig. 5.10.

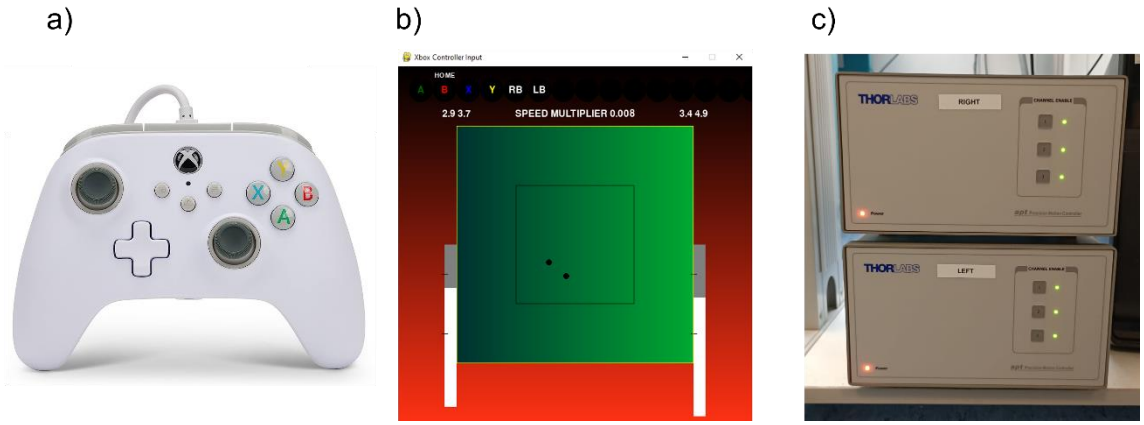

Figure 5.10. a) XBOX controller used to control the program. b) Program interface to control the motors. c) Motors that control the positioners.

Finally, Fig. 5.11 shows a zoom to the area where the sample is located (DUT) during the measurements. In addition to the sample, the optical fibre used can be clearly seen.

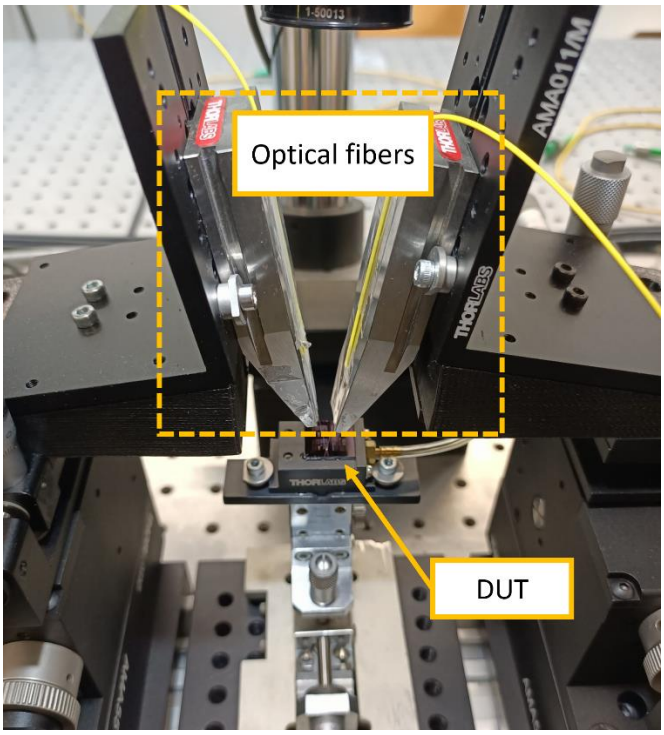

Figure 5.11. Zoom of the DUT showing the optical fibres.

5.6 Experiment results

As explained above, the purpose of the experiment is to measure the losses contributed by the ITO patch to the complete structure. For this purpose, the set-up explained in the previous section has been prepared to measure the output power (P_{out}) of the structure (grating on the right). To obtain the losses, it is only necessary to subtract the reference P_{out} from the P_{out} of each device. This will give the losses as a function of the length of the ITO layer. In addition, thanks to the collaboration mentioned above with Nottingham Trent University (United Kingdom), it has been possible to tune the ENZ region around 1550 nm, so that a wavelength-dependent scan will also

be performed to try to appreciate the ENZ resonance. The laser has been configured to work with a range of 1540 to 1580 nm.

With all this, the P_{out} of each of the devices is obtained. By processing the data in Matlab, Fig. 5.12 is obtained. This clearly shows the effect of the ITO layer. The reference waveguide has the highest output power. As the ITO is added and the patch becomes longer this power decreases considerably. This is the desired effect as the ITO in the ENZ region confines the field inside where the light is absorbed. It is also important to note that the evolution of the losses of the devices with ITO is linear and proportional to the length of the ITO.

In addition, another effect can be seen in the ITO-containing structures. They all have less P_{out} at wavelengths (λ) around 1540 nm. This indicates that the ITO layer confines more field around this wavelength due to the ENZ effect. Thereby, the ENZ is not perfectly tunned at 1550 nm but slightly lower, approximately 1540 nm.

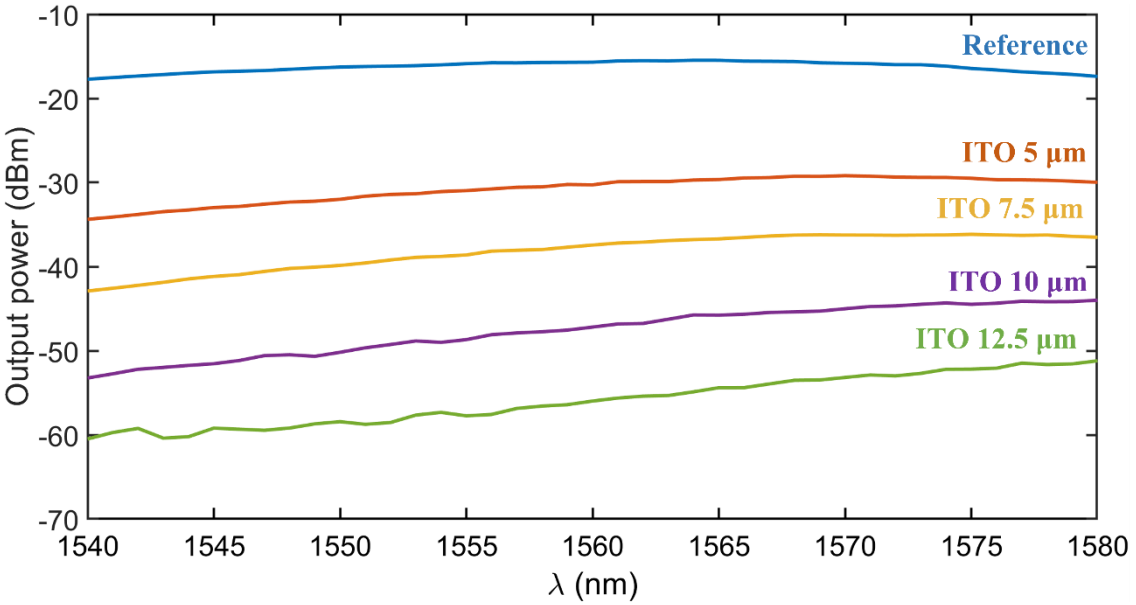

Figure 5.12. Output power (P_{out}) as a function of wavelength (nm) for each device (reference without ITO and those with 5, 7.5, 10 and 12.5 µm ITO).

With the data obtained from the P_{out}, the losses provided by the ITO are obtained. As mentioned above, to do this it is only necessary to obtain the difference between the structure with ITO and the reference structure (silicon waveguide). By doing this process in each of the structures, Fig. 5.13 is obtained. It can be seen that the longer the length of the ITO patch, the higher the losses. This is related to what was mentioned above, since the longer the ITO, the lower the output power (more losses). It can also be seen that for wavelengths of 1540 nm the material has more losses than at 1550 nm, which again shows that the ENZ is slightly displaced towards lower wavelengths.

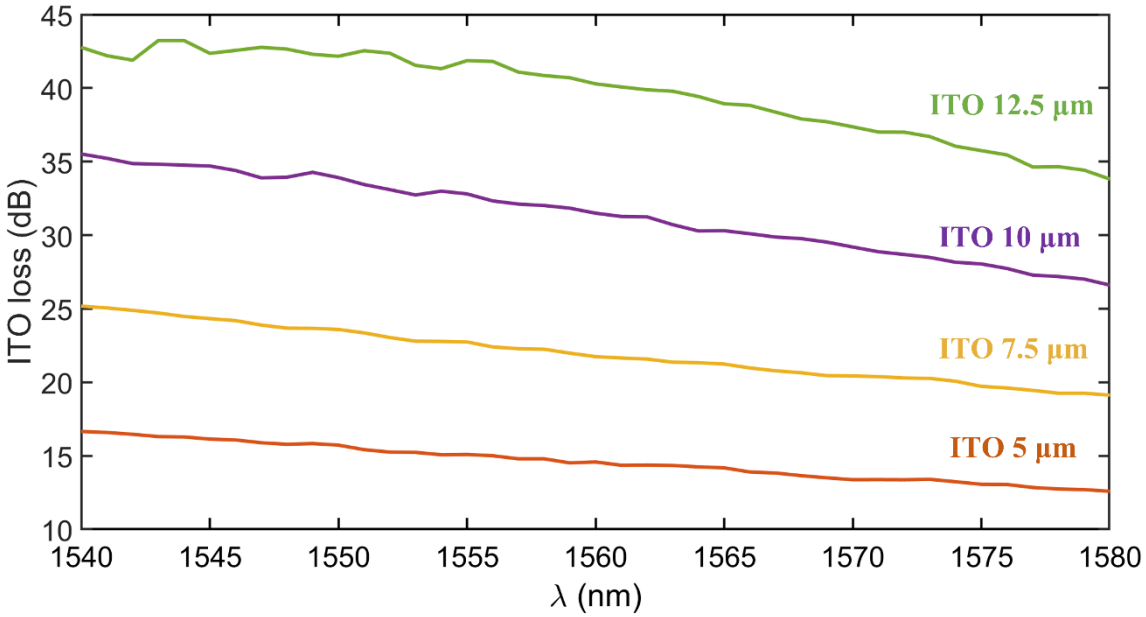

Figure 5.13. ITO losses (dB) as a function of wavelength (nm) for each device (5, 7.5, 10 and 12.5 µm of ITO).

Once the previous losses have been obtained, it only remains to focus on the wavelength at which the devices should work, 1550 nm. To do this, the ITO losses for each case are extracted from Fig. 5.13, but only at 1550 nm. The representation of these values as a function of the ITO length can be seen in Fig. 5.14. In addition to the isolated points for each length, a linear regression has been performed with the help of Matlab with the final objective of obtaining the κ_{eff} of the structures with the ITO (imaginary part of the complex index). For this purpose, as mentioned above, a linear regression is carried out, obtaining the straight line shown in Fig. 5.14. The slope of this line is b = 3.58 dB/µm.

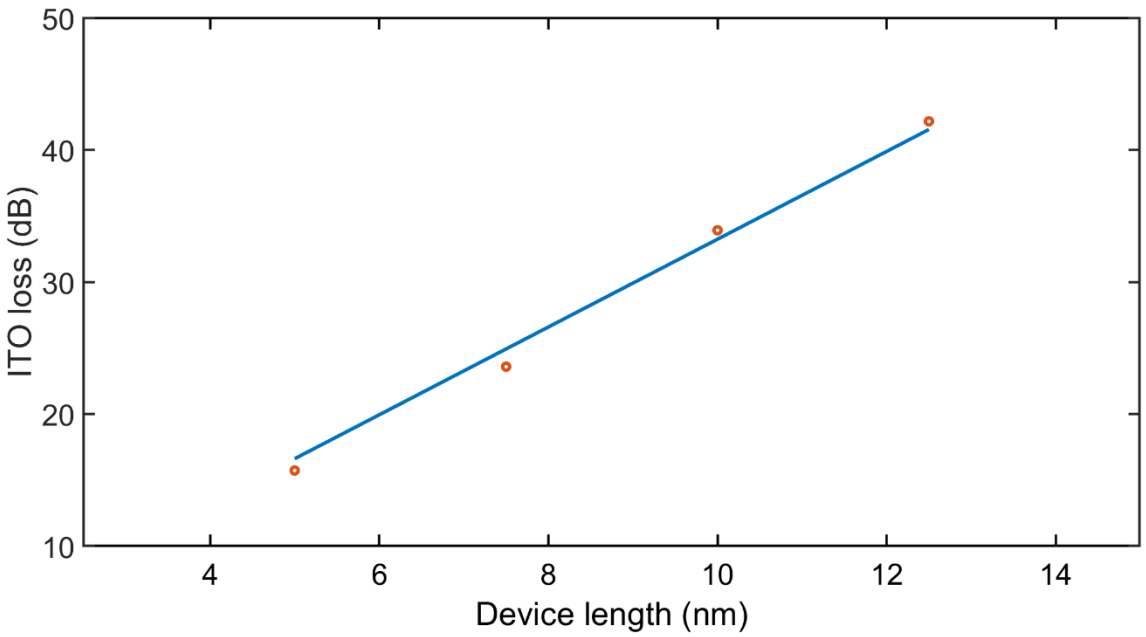

Figure 5.14. ITO losses at 1550 nm of the structures and linear regression with these points.

Therefore, from the equation of the propagation losses, we can estimate κ_{eff} :

$$\kappa_{eff} = \frac{b * \lambda}{20log_{10}(e) * 2\pi} \tag{5.1}$$

From equation 5.1 we obtain a κ_{eff} of 0.10 (± 0.02 assigned of estimated error) to the actual structures that have been fabricated. To determine if the data obtained in the experiment are consistent or not, the κ_{eff} has also been obtained by simulation.

The structure with the 50 nm ITO layer (Fig. 5.1 b) has been simulated in the RSoft FEMSIM environment to determine the optical constants of the ITO and its carrier concentration. Such simulation predicts the optical losses extracted from the fit of the losses in Fig. 5.15 of κ_{eff} = 0.10 ± 0.02. From simulations we obtain a compatible result of n_{eff} = 1.55 and a κ_{eff} = 0.08 at a wavelength of 1550 nm, together with a carrier concentration of N = 9.8 10^{20} cm^{-3} (see the complex refractive index versus carrier concentration shown in Fig. 5.15). These data obtained with the simulation are compatible with those obtained with the simulations and it can be concluded that the measured sample agrees with the expected results.

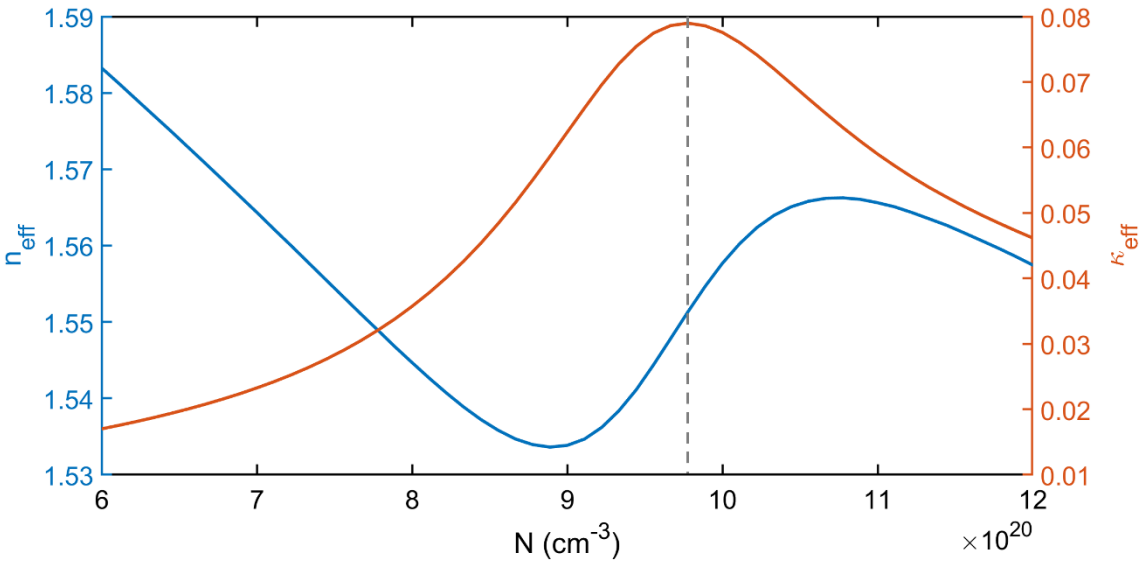

Figure 5.15. Complex index vs carrier concentration for the simulation of the fabrication structure.

Chapter 6. Conclusions and future work

6.1 Conclusions

Current applications require a very high switching speed, but at the same time the aim is to make the devices as compact as possible. Electronics cannot achieve this, so this project presents photonic integrated circuits (PICs) as a replacement. Transparent conductive oxides (TCOs) are materials suitable for the development of PICs (CMOS-compatible) in the near infrared (NIR). These materials are the focus of the work because of the possibilities they offer by providing drastic refractive index changes depending on their carrier concentration. This in turn allows them to be modified by the bias voltage. These materials have a special region called the ENZ region where they can provide a drastic variation of the refractive index. In particular, indium tin oxide (ITO) has been used for the initial design. A hybrid ITO/Si modulator has been designed which allows modulation in both amplitude and phase by altering the carrier concentration or bias voltage applied to the capacitor.

The design consists of a standard Si waveguide (500 x 220 nm) on which a 10 nm layer of ITO, a 10 nm layer of oxide (HfO_2) and 100 nm of metal (Au) are located. To determine the behaviour of the ITO layer and therefore of the whole structure, the Drude model is used. From it, it is determined that for the design made to obtain the ENZ region, a voltage of 3.5 V is necessary. In addition, the evolution of the complex index of the ITO layer is also determined as a function of V_b and N. With this, by means of RSoft FEMSIM, the evolution of the complex effective index of the structure is obtained as a function of V_b. In this case, the ENZ region coincides with a V_b = 3.7 V. Subsequently, two FOMs ($FOM^{\Delta\phi}$ and FOM^{κ}) are defined in order to determine the optimal oxide thickness. It follows that the optimum thickness is 10 nm.

The maximums provided by the FOMs are the voltage values at which device operation is optimal depending on whether it is intended to modulate in phase or amplitude. The V_b related to the FOM^{κ} is 3.7 V (ENZ region) while for the $FOM^{\Delta\phi}$ it is 7 V. The power consumed at each of these points is 75 and 270 fJ respectively. The design has a bandwidth of approximately 20 GHz.

In addition, a complex structure formed by the concatenation of these base modulators has been designed. The arrayed multilength ITO/Si modulator presents a large number of complex combinations in phase shift and loss making it a promising device for neural network weights. As more and longer modulators are added to the structure, all possible combinations in phase shift are achieved, although the losses also increase.

Subsequently, the base modulator has been taken and the ITO has been modified by CdO, a TCO with higher mobility. The performance of the device is improved in almost all aspects. However, it is not proposed to go further into this material due to the impossibility of working with it at the NTC (Nanophotonics Technology Center), where this project has been carried out. Nevertheless, it is stated that the mobility (μ) is directly related to the performance of the device, since the higher the μ, the better the performance of the modulator.

Finally, an experimental part has been carried out in which a more simplified design has been used to determine the performance of the ITO layer. The sample is a silicon waveguide on which 50 nm of ITO was deposited on top with different lengths. The ENZ wavelength of ITO was tuned at 1550 nm with a novel annealing technique known as Reactive Laser Annealing. By means of experimental measurements, the effect of having ENZ-resonant ITO on the structure is verified and it is shown that the longer the ITO length, the greater the effect (higher losses, higher mode confinement in the ITO layer). Experimentally, a $\kappa eff = 0.10 \pm 0.02$ with insertion losses (IL) of 2.5 dB/μm is determined. To demonstrate the correct performance of the sample, the measured structure has been simulated, obtaining a $\kappa_{eff} = 0.08$ for a carrier concentration of $0.98 \cdot 10^{21}\ cm^{-3}$. Since the κ_{eff} are similar and of the same order, it is assumed that the experimentally obtained results are adequate. For the fabrication of the sample the NTC has collaborated with a

group based on the School of Science and Technology, Nottingham Trent University (United Kingdom) that performed the ReLA process and the sputtering of the ITO.

6.2 Future work

Once the correct operation of the sample consisting only of the ITO layer has been demonstrated and the ReLA process has been demonstrated to be able to tune the carrier concentration of the ITO so that the ENZ wavelength is resonant at around 1550 nm, the lines of future work that could be tackled through this project will be focused on:

1. Fabrication of the sample with the complete capacitor structure in order to verify what has been theorised with the simulations. To be able to build a device such as this one, the fabrication of the oxide and metal layers should be introduced in the workflow and the fabrication must be optimized. Additionally, the electrodes must also be developed to be able to create the electrical contacts to bias the capacitor structure.
2. Experimental study of the optoelectronic modulator with a more advanced setup that includes time-resolved measurements for amplitude and phase modulation. For the phase modulation, an indirect phase detection structure like a Mach–Zehnder interferometer must be included in the design.
3. Study of more advanced device geometries that implement other optical operations with light and exploit their performance for emerging application fields such as neuromorphic computing.

Chapter 7. Bibliography

[1] J. Navarro-Arenas, J. Parra, and P. Sanchis, "Ultrafast all-optical phase switching enabled by epsilon-near-zero materials in silicon," *Opt. Express*, vol. 30, no. 9, pp. 14518–14529, Apr. 2022, doi: 10.1364/OE.454181.

[2] G. Lifante, *Integrated Photonics: Fundamentals*. 2003.

[3] L. Pavesi, "Thirty Years in Silicon Photonics: A Personal View," *Front Phys*, vol. 9, 2021, doi: 10.3389/fphy.2021.786028.

[4] H. Wong, V. Filip, C. K. Wong, and P. S. Chung, "Silicon integrated photonics begins to revolutionize," *Microelectronics Reliability*, vol. 47, no. 1, pp. 1–10, 2007, doi: https://doi.org/10.1016/j.microrel.2006.01.002.

[5] H. Föll, S. Langa, J. Carstensen, M. Christophersen, and I. M. Tiginyanu, "Pores in III–V Semiconductors," *Advanced Materials*, vol. 15, no. 3, pp. 183–198, 2003, doi: https://doi.org/10.1002/adma.200390043.

[6] S. J. Ben Yoo, "Hybrid integrated photonic platforms: opinion," *Opt Mater Express*, vol. 11, no. 10, pp. 3528–3534, 2021, doi: 10.1364/OME.438778.

[7] B. Jalali and S. Fathpour, "Silicon Photonics," *Journal of Lightwave Technology*, vol. 24, no. 12, pp. 4600–4615, 2006, doi: 10.1109/JLT.2006.885782.

[8] J. Navarro-Arenas, J. Parra, and P. Sanchis, "Comparative performance evaluation of transparent conducting oxides with different mobilities for all-optical switching in silicon," *IEEE J Quantum Electron*, p. 1, 2023, doi: 10.1109/JQE.2023.3264774.

[9] J. Wu, Z. T. Xie, Y. Sha, H. Y. Fu, and Q. Li, "Epsilon-near-zero photonics: infinite potentials," *Photon. Res.*, vol. 9, no. 8, pp. 1616–1644, Aug. 2021, doi: 10.1364/PRJ.427246.

[10] M. Z. Alam, I. De Leon, and R. W. Boyd, "Large optical nonlinearity of indium tin oxide in its epsilon-near-zero region," *Science (1979)*, vol. 352, no. 6287, pp. 795–797, 2016, doi: 10.1126/science.aae0330.

[11] M. G. Silveirinha and N. Engheta, "Theory of supercoupling, squeezing wave energy, and field confinement in narrow channels and tight bends using epsilon near-zero metamaterials," *Phys Rev B*, vol. 76, no. 24, p. 245109, Dec. 2007, doi: 10.1103/PhysRevB.76.245109.

[12] X. Niu, X. Hu, S. Chu, and Q. Gong, "Epsilon-Near-Zero Photonics: A New Platform for Integrated Devices," *Adv Opt Mater*, vol. 6, no. 10, p. 1701292, 2018, doi: https://doi.org/10.1002/adom.201701292.

[13] R. Maas, J. Parsons, N. Engheta, and A. Polman, "Experimental realization of an epsilon-near-zero metamaterial at visible wavelengths," *Nat Photonics*, vol. 7, no. 11, pp. 907–912, 2013, doi: 10.1038/nphoton.2013.256.

[14] I. C. Reines, M. G. Wood, T. S. Luk, D. K. Serkland, and S. Campione, "Compact epsilon-near-zero silicon photonic phase modulators," *Opt. Express*, vol. 26, no. 17, pp. 21594–21605, Aug. 2018, doi: 10.1364/OE.26.021594.

[15] M. Sojib, D. Fomra, V. Avrutin, Ü. Özgür, and N. Kinsey, "Optimizing epsilon-near-zero based plasmon assisted modulators through surface-to-volume ratio," *Opt Express*, vol. 30, no. 11, pp. 19781–19794, 2022, doi: 10.1364/OE.457063.

[16] D. Gao and Z. Zhou, "Silicon-based optoelectronics: progress towards large scale optoelectronic integration and applications," *Frontiers of Optoelectronics*, vol. 15, no. 1, p. 27, 2022, doi: 10.1007/s12200-022-00030-7.

[17] V. J. Sorger, N. D. Lanzillotti-Kimura, R.-M. Ma, and X. Zhang, "Ultra-compact silicon nanophotonic modulator with broadband response," vol. 1, no. 1, pp. 17–22, 2012, doi: doi:10.1515/nanoph-2012-0009.

[18] G. T. Reed, G. Mashanovich, F. Y. Gardes, and D. J. Thomson, "Silicon optical modulators," *Nat Photonics*, vol. 4, no. 8, pp. 518–526, 2010, doi: 10.1038/nphoton.2010.179.

[19] A. P. Vasudev, J.-H. Kang, J. Park, X. Liu, and M. L. Brongersma, "Electro-optical modulation of a silicon waveguide with an ``epsilon-near-zero'' material," *Opt. Express*, vol. 21, no. 22, pp. 26387–26397, Nov. 2013, doi: 10.1364/OE.21.026387.

[20] N. Kinsey, C. DeVault, J. Kim, M. Ferrera, V. M. Shalaev, and A. Boltasseva, "Epsilon-near-zero Al-doped ZnO for ultrafast switching at telecom wavelengths," *Optica*, vol. 2, no. 7, pp. 616–622, Jul. 2015, doi: 10.1364/OPTICA.2.000616.

[21] Z. Lu, W. Zhao, and K. Shi, "Ultracompact Electroabsorption Modulators Based on Tunable Epsilon-Near-Zero-Slot Waveguides," *IEEE Photonics J*, vol. 4, no. 3, pp. 735–740, 2012, doi: 10.1109/JPHOT.2012.2197742.

[22] S. Mohammadi-Pouyan, M. Miri, and M. H. Sheikhi, "Efficient binary and QAM optical modulation in ultra-compact MZI structures utilizing indium-tin-oxide," *Sci Rep*, vol. 12, no. 1, p. 8129, 2022, doi: 10.1038/s41598-022-12298-y.

[23] V. E. Babicheva, A. Boltasseva, and A. V Lavrinenko, "Transparent conducting oxides for electro-optical plasmonic modulators," vol. 4, no. 2, pp. 165–185, 2015, doi: doi:10.1515/nanoph-2015-0004.

[24] Z. Lu, W. Zhao, and K. Shi, "Ultracompact Electroabsorption Modulators Based on Tunable Epsilon-Near-Zero-Slot Waveguides," *IEEE Photonics J*, vol. 4, no. 3, pp. 735–740, 2012, doi: 10.1109/JPHOT.2012.2197742.

[25] A. V Krasavin and A. V Zayats, "Photonic Signal Processing on Electronic Scales: Electro-Optical Field-Effect Nanoplasmonic Modulator," *Phys Rev Lett*, vol. 109, no. 5, p. 53901, Jul. 2012, doi: 10.1103/PhysRevLett.109.053901.

[26] A. Melikyan *et al.*, "Surface plasmon polariton absorption modulator," *Opt Express*, vol. 19, no. 9, pp. 8855–8869, 2011, doi: 10.1364/OE.19.008855.

[27] V. J. Sorger, N. D. Lanzillotti-Kimura, R.-M. Ma, and X. Zhang, "Ultra-compact silicon nanophotonic modulator with broadband response," vol. 1, no. 1, pp. 17–22, 2012, doi: doi:10.1515/nanoph-2012-0009.

[28] A. K. Jain, J. Mao, and K. M. Mohiuddin, "Artificial neural networks: a tutorial," *Computer (Long Beach Calif)*, vol. 29, no. 3, pp. 31–44, 1996, doi: 10.1109/2.485891.

[29] G. Ramirez-Gargallo, M. Garcia-Gasulla, and F. Mantovani, "TensorFlow on State-of-the-Art HPC Clusters: A Machine Learning use Case," in *2019 19th IEEE/ACM International Symposium on Cluster, Cloud and Grid Computing (CCGRID)*, 2019, pp. 526–533. doi: 10.1109/CCGRID.2019.00067.

[30] K. Liao, T. Dai, Q. Yan, X. Hu, and Q. Gong, "Integrated Photonic Neural Networks: Opportunities and Challenges," *ACS Photonics*, Feb. 2023, doi: 10.1021/acsphotonics.2c01516.

[31] R. Amin *et al.*, "ITO-based electro-absorption modulator for photonic neural activation function," *APL Mater*, vol. 7, no. 8, p. 081112, Aug. 2019, doi: 10.1063/1.5109039.

[32] A. N. Tait *et al.*, "Neuromorphic Silicon Photonic Networks," Nov. 2016, doi: 10.1038/s41598-017-07754-z.

[33] C. Sire, S. Blonkowski, M. J. Gordon, and T. Baron, "Statistics of electrical breakdown field in HfO2 and SiO2 films from millimeter to nanometer length scales," *Appl Phys Lett*, vol. 91, no. 24, p. 242905, Dec. 2007, doi: 10.1063/1.2822420.

[34] S. Mohammadi-Pouyan, M. Miri, and M. H. Sheikhi, "Efficient binary and QAM optical modulation in ultra-compact MZI structures utilizing indium-tin-oxide," *Sci Rep*, vol. 12, no. 1, p. 8129, 2022, doi: 10.1038/s41598-022-12298-y.

[35] S. Zhu, G. Q. Lo, and D. L. Kwong, "Design of an ultra-compact electro-absorption modulator comprised of a deposited TiN/HfO2/ITO/Cu stack for CMOS backend integration," *Opt. Express*, vol. 22, no. 15, pp. 17930–17947, Jul. 2014, doi: 10.1364/OE.22.017930.

[36] R. Secondo, J. Khurgin, and N. Kinsey, "Absorptive loss and band non-parabolicity as a physical origin of large nonlinearity in epsilon-near-zero materials," *Opt. Mater. Express*, vol. 10, no. 7, pp. 1545–1560, Jul. 2020, doi: 10.1364/OME.394111.

[37] V. J. Sorger, N. D. Lanzillotti-Kimura, R.-M. Ma, and X. Zhang, "Ultra-compact silicon nanophotonic modulator with broadband response," vol. 1, no. 1, pp. 17–22, 2012, doi: doi:10.1515/nanoph-2012-0009.

[38] B. Zhou, E. Li, Y. Bo, and A. X. Wang, "High-Speed Plasmonic-Silicon Modulator Driven by Epsilon-Near-zero Conductive Oxide," *Journal of Lightwave Technology*, vol. 38, no. 13, pp. 3338–3345, 2020, doi: 10.1109/JLT.2020.2979192.

[39] R. Amin *et al.*, "Heterogeneously integrated ITO plasmonic Mach–Zehnder interferometric modulator on SOI," *Sci Rep*, vol. 11, no. 1, p. 1287, 2021, doi: 10.1038/s41598-020-80381-3.

[40] Y. Gui *et al.*, "100 GHz micrometer-compact broadband monolithic ITO Mach–Zehnder interferometer modulator enabling 3500 times higher packing density," vol. 11, no. 17, pp. 4001–4009, 2022, doi: doi:10.1515/nanoph-2021-0796.

[41] E. Sachet *et al.*, "Dysprosium-doped cadmium oxide as a gateway material for mid-infrared plasmonics," *Nat Mater*, vol. 14, no. 4, pp. 414–420, 2015, doi: 10.1038/nmat4203.

[42] T. Usui, C. A. Donnelly, M. Logar, R. Sinclair, J. Schoonman, and F. B. Prinz, "Approaching the limits of dielectric breakdown for SiO2 films deposited by plasma-enhanced atomic layer deposition," *Acta Mater*, vol. 61, no. 20, pp. 7660–7670, 2013, doi: https://doi.org/10.1016/j.actamat.2013.09.003.

[43] S. Song, T. Yang, J. Liu, Y. Xin, Y. Li, and S. Han, "Rapid thermal annealing of ITO films," *Appl Surf Sci*, vol. 257, no. 16, pp. 7061–7064, 2011, doi: https://doi.org/10.1016/j.apsusc.2011.03.009.

[44] J. A. Hillier *et al.*, "Reactive laser annealing of indium tin oxide: implications to crystal structure, defect composition, and plasma energy," *Opt. Mater. Express*, vol. 12, no. 11, pp. 4310–4327, Nov. 2022, doi: 10.1364/OME.464918.